The Mineral Chemistry of Chlorites and Its Relationship with Uranium Mineralization from Huangsha Uranium Mining Area in the Middle Nanling Range, SE China

Dehai Wu [1],* , **Jiayong Pan [1],*, Fei Xia [1], Guangwen Huang [2] and Jing Lai [3]**

[1] State Key Laboratory of Nuclear Resources and Environment, East China University of Technology, Nanchang 330013, China; fxia@ecit.cn
[2] Qinghai Geological Survey Institute, Xi'ning 810012, China; gwhuang1991@163.com
[3] Research Institute NO. 290, CNNC, Shaoguan 512026, China; jinglai1994@163.com
* Correspondence: dehaiwu@163.com (D.W.); jypan@ecit.cn (J.P.); Tel.: +86-794-8258359 (D.W.); +86-794-8258359 (J.P.)

Abstract: The Huangsha uranium mining area is located in the Qingzhangshan uranium-bearing complex granite of the Middle Nanling Range, Southeast China. This uranium mining area contains three uranium deposits (Liangsanzhai, Egongtang, and Shangjiao) and multiple uranium occurrences, showing favorable mineralization conditions and prospecting potential for uranium mineral resources. Chloritization is one of the most important alteration types and prospecting indicators in this mining area. This study aims to unravel the formation environment of chlorites and the relationship between chloritization and uranium mineralization, based on detailed field work and petrographic studies of the wallrock and ore samples from the Huangsha uranium mining area. An electron probe microanalyzer (EPMA) was used in this study to analyze the paragenetic association, morphology, and chemical compositions of chlorite, to classify chemical types and to calculate formation temperatures and $n(Al)/n(Al + Mg + Fe)$ values of chlorite. The formation mechanism and the relationship with uranium mineralization of the uranium mining area are presented. Some conclusions from this study are: (1) There are five types of chlorites, including the chlorite formed by the alteration of biotite (type-I), by the metasomatism of feldspar with Fe–Mg hydrothermal fluids (type-II), chlorite vein/veinlet filling in fissures (type-III), chlorite closely associated with uranium minerals (type-IV), and chlorite transformed from clay minerals by adsorbing Mg- and Fe-components (type-V). (2) The chlorite in the Huangsha uranium mining area belongs to iron-rich chlorite and is mainly composed of chamosite, partly clinochlore, which are the products of multiple stages of hydrothermal action. The original rocks are derived from argillite, and their formation temperatures vary from 195.7 °C to 283.0 °C, with an average of 233.2 °C, suggesting they formed under a medium to low temperature conditions. (3) The chlorites were formed under reducing conditions with low oxygen fugacity and relatively high sulfur fugacity through two formation mechanisms: dissolution–precipitation and dissolution–migration–precipitation; (4) The chloritization provided the required environment for uranium mineralization, and promoted the activation, migration, and deposition of uranium.

Keywords: Chlorites; Electron probe microanalyzer; Formation temperature; Uranium metallogenesis; Huangsha uranium mining area

1. Introduction

Chlorite (a group which consists of 13 mineral species) is widely distributed in different rock and geological environments. It is one of the common minerals formed in rocks with low–medium temperature metamorphism, diagenesis, and in the process of hydrothermal alteration of copper, uranium, and gold deposits [1–7]. Through the study of chlorites in various geothermal and hydrothermal systems, many scholars have summarized the empirical formulas for estimating the physical and chemical formation conditions of chlorite by using the composition and structural change characteristics of chlorite, and established a series of quantitative research models [7–14]. For example, MacDowell and Elders (1980) [15] show that Si^{IV}-Al^{IV} in chlorite is negatively correlated with diagenetic depth. Cathelineau (1988) [8] found that there is a positive correlation between Al^{IV}-T (Temperature) in chlorite by analyzing the relationship between composition and temperature of chlorite in the geothermal systems of Los Azufres and Salton Sea in Mexico and a chlorite solid solution geothermometer was proposed. However, some controversies still exist; Caritat et al. (1993) [2] performed a systematic comparative study of four chlorite geothermometers, which are proposed by Hayes (1970) [16], Walshe (1986) [17], Cathelineau (1988) [8], and Hutcheon (1990) [18]. The chemical composition of chlorite varies greatly in different geological environments, and the main physical and chemical parameters (such as the temperature, oxygen fugacity, pH value of the aqueous solution, Fe/(Fe + Mg) of the whole rock, etc.) affect its chemical composition. Thus, these four methods of chlorite geothermometry have certain applicable conditions and limitations and should be used in combination with alternative methods to estimate paleotemperatures [2]. In this regard, Rause-Colom et al. (1991) [19], Nieto (1997) [20], and Battaglia et al. (1999) [11] have revised the original chlorite geothermometer, which has been more widely recognized and applied by geologists.

The North Guangdong–South Jiangxi province is one of the most typical granite-type uranium ore fields in China. It is also an important part of the W–Sn–Mo–Be–REE–(Pb–Zn–Au) polymetallic metallogenic belt in the Middle Nanling Range [21–25]. Huangsha uranium mining area is located in the south-central part of Qingzhangshan uranium-bearing complex granites in the Middle Nanling Range. The mining area contains three uranium deposits (Liangsanzhai, Egongtang, and Shangjiao uranium deposits in the north–west, middle, and south-west of the mining area, respectively). Over the past half century, researchers have carried out relevant studies on the geological characteristics, metallogenic conditions, ore-controlling factors, metallogenic mechanisms, and metallogenic prediction of the Huangsha uranium mining area [26–28]. There are few studies on wallrock alteration in this area, which are mainly concentrated on the major and trace element geochemical characteristics. For example, Mou et al. (2016) [29] analyzed major and trace elements in rock samples with different alteration types (chloritization, hydromica, fluorination, and hematitization), and discussed the geochemical characteristics of hydrothermal alteration and the law of element migration in the mining area. Wu et al. (2018) [30] performed a comparative study of the geochemical characteristics of trace elements and rare earth elements for various rocks (granites, dolerites, and uranium ores) from Shangjiao uranium deposit, and established a metallogenic model.

The hydrothermal uranium deposits are characterized by intense hydrothermal alteration, in which chloritization is an important alteration type before and during the metallogenic stage, which is closely related to uranium mineralization [4,5]. Chloritization is a very important prospecting indicator for uranium deposits, especially in the Huangsha uranium mining area. A thorough study of the relationship between chloritization and uranium mineralization will help better understand the genetic mechanism of the deposit in this mining area. The representative chlorite samples of different occurrences and genesis in Huangsha uranium mining area were collected. On the basis of detailed rock-mineral identification, the chemical compositions of chlorites were analyzed by EPMA (Electron probe microanalyzer). The formation environment of chlorites and the relationship between chloritization and uranium mineralization were discussed.

2. Geological Background

Huangsha uranium mining area is located in the south-central part of Qingzhangshan granitic pluton in the middle of Nanling metallogenic belt (Figure 1A,B) [31,32]. The belt is in the southwestern border of the Cathaysia paleocontinent, adjacent to the joint zone of the Hercynian-Indosinian sink of the Hunan–Guangxi–North Guangdong provinces and the Caledonian rise of the Fujian–Jiangxi–Guangdong provinces. The Qingzhangshan granitic pluton formed in the Middle Triassic–Late Jurassic. It has a north–south distribution area of about 500 km^2 (Figure 1B,C) [32,33]. The main body of Qingzhangshan granitic pluton formed at the Middle Triassic (medium-coarse to medium-grained porphyritic biotite granite with a formation age of about 241.0 Ma) [34–37]; Late Jurassic granite (medium-fine grained two-mica granite with a formation age of about 156.0 Ma) [33–37] and Late Jurassic syenite (medium-grained quartz syenite with a formation age of about 149.4 Ma and features of A-type granite) [33] occur with stocks and dikes. The granitic pluton intruded into Cambrian–Jurassic slate, phyllite, and carbonaceous argillaceous shale, and hornfels developed widely at the contact segment. Dolerite veins and silicified fault zones have developed in the granitic pluton.
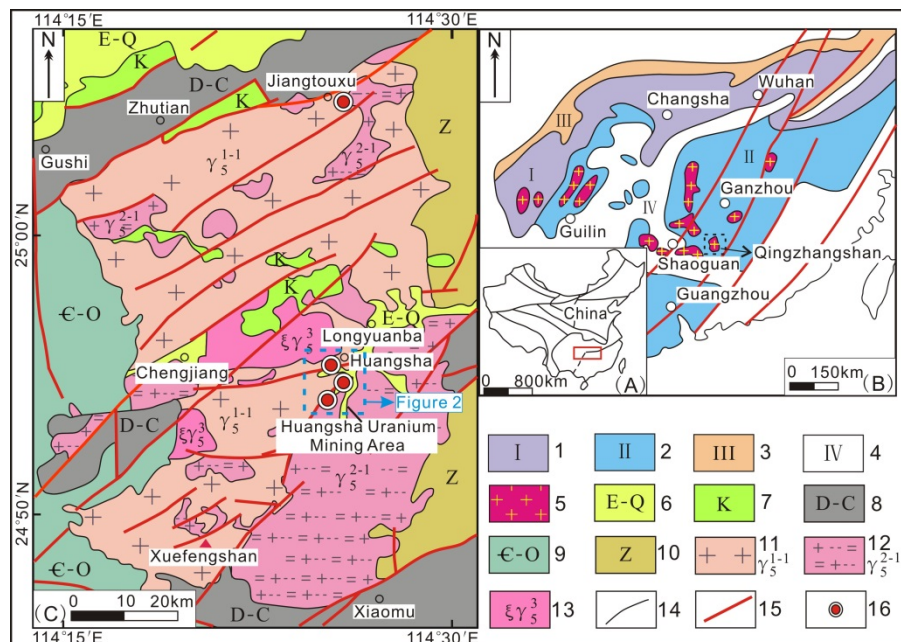
Figure 1. (**A**) Simplified geological map of China; (**B**) Tectonic location and (**C**) Geological sketch of Qingzhangshan complex pluton. Note: Figure 1A modified from Yan et al. (2003) [31], Figure 1B modified from Zhang and Zhang (1991) [32], Figure 1C modified from Tao et al. (2013) [33] 1—Jiangnan anticline; 2—Caledonian rise of Fujian–Jiangxi–Guangdong; 3—Margin of Late Caledonian rise; 4—Hercynian-Indosinian sink of Hunan–Guangxi–North Guangdong; 5—Uranium-bearing granite; 6—Paleogene-Quaternary; 7—Cretaceous; 8—Devonian–Carboniferous; 9—Cambrian–Ordovician; 10—Sinian; 11—Middle Triassic granite; 12—Late Jurassic granite; 13—Late Jurassic quartz-syenite; 14—Lithologic boundary; 15—Fault zone; 16—Uranium deposit.

The uranium deposits in the Huangsha uranium mining area are of typical postmagmatic hydrothermal origin and are hydrothermal vein type uranium deposits. The Middle Triassic pale red medium-coarse to medium-grained porphyritic biotite granite and the Late Jurassic medium-fine-grained two-mica granite are widely exposed in the area. Medium-coarse to medium-grained porphyritic biotite granites with pink feldspar phenocrysts are the main host rock in the Huangsha uranium mining area (Figure 2A). Late basic magma intruded along faulted structures, forming NW, NE, and EW trending dolerite veins with a width of 0.5–20 m. The veins extend hundreds to thousands of meters toward the trend of dolerite veins, with the characteristics of expansion, contraction, thinning-out,

and recurrence, and are densely integrated into an oblique, equidistant group distribution. The nearly EW-trending Huangsha and Shangzhukeng fault zones are large in scale, parallel to each other, and in opposition to the trend across the uranium area, which both comprise the EW-trending Huangsha fault depression zone and control the distribution of uranium deposits (uranium occurrences) in the Huangsha uranium mining area.
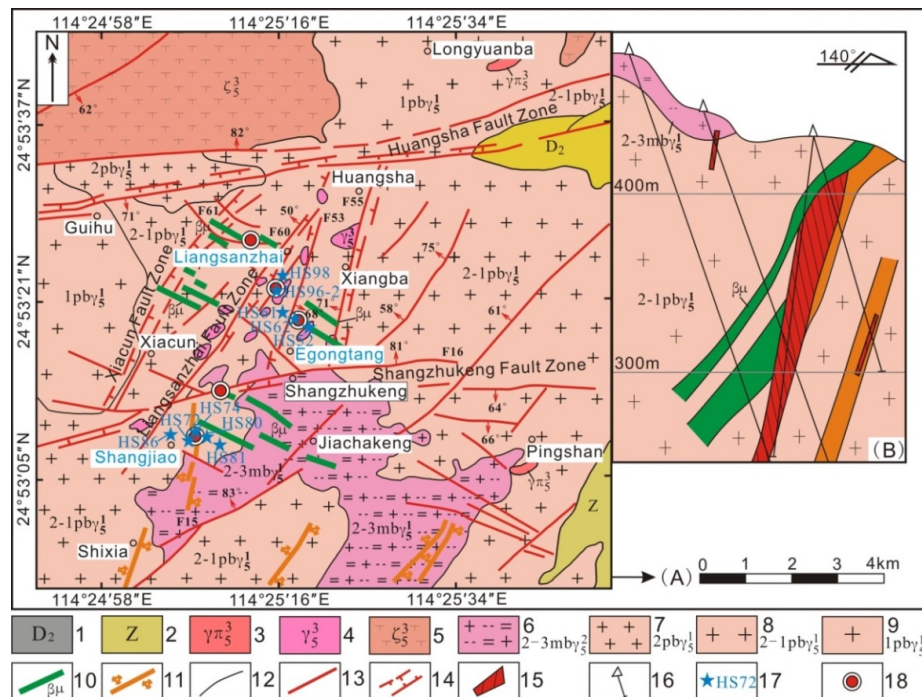
Figure 2. (**A**)—Geological map for the Huangsha uranium mining area with sampling positions and (**B**)—Geological section from Shangjiao uranium deposit. Note: 1—Middle Devonian System; 2—Sinian; 3—Granite-porphyry; 4—Late Jurassic fine-grained granite; 5—Late Jurassic Syenite and quartz-syenite; 6—Late Jurassic medium-fine grained two-mica granite; 7—Middle Triassic medium -grained porphyritic biotite granite; 8—Middle Triassic medium -coarse grained porphyritic biotite granite; 9—Middle Triassic coarse-grained porphyritic biotite granite; 10—Diabase dike; 11—Silicificational fracture zone; 12—Lithologic boundary; 13—Fault; 14—Fault zone; 15—Uranium ore; 16—Drill hole; 17—Sampling location and code; 18—Uranium deposit.

The ore bodies are veined, reticulated, lenticular, and pod-like in the Huangsha uranium mining area, most of which occur at the intersection of silicified faults and dolerite veins (Figure 2B). Their mineralization characteristics are similar to those of Xiazhuang "intersection" type uranium mineralization. The uranium deposits (uranium occurrences) occur at the intersection between the WNW-trending dolerite dykes and the NNE-trending faults within the Triassic granites of the eastern Guidong batholith, Southeast China [38–40]. The electron microprobe U-Th-Pb pitchblende dating yields about 97 Ma and 72 Ma (data will be published in another article), which suggests that there have been at least two uranium metallogenic events in the Huangsha uranium mining area. Ores are grape-like, kidney-like, and have microcrystalline texture with fine veins, stockwork, and blocky structure. The ore minerals are mainly pitchblende, followed by coffinite. Metallic minerals are pyrite, galena, and sphalerite. Gangue minerals are chalcedony, microcrystalline quartz, fine-grained quartz, fluorite, and calcite. The secondary uranium minerals are uranotile, chalcolite, and calcouranite. Near-ore alterations are mainly hematization, silicification, and fluoritization, while far-ore alterations are mainly hydromicazation, chloritization, pyritization, and carbonation. From the center of the ore body outward, silicification, hematitization, fluoritization, chloritization, and hydromicazation are gradually weakened (Figure 3).
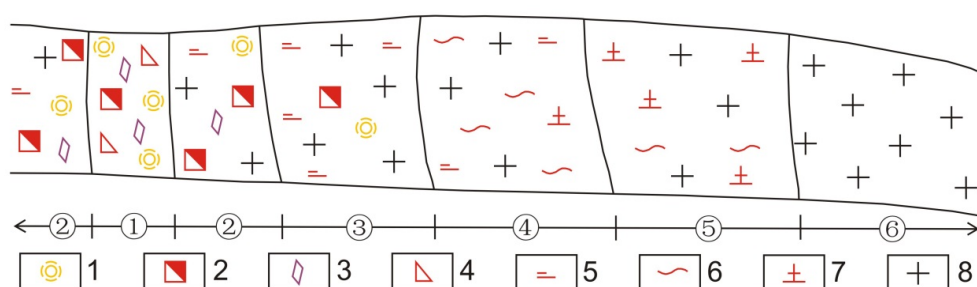
Figure 3. Sketch of alteration zone in the Huangsha uranium mining area. ①—Silicification alteration zone; ②—Hematization alteration zone; ③—Hydromicazation alteration zone; ④—Chloritization alteration zone; ⑤—Kaolinization alteration zone; ⑥—Fresh granite. 1—Silicification; 2—Hematization; 3—Fluoritization; 4—Tectonic breccia; 5—Hydromicazation; 6—Chloritization; 7—Kaolinization; 8—Granite.

The representative altered rocks and their petrographic characteristics in Huangsha uranium mining area are as follows.

The medium-grained porphyritic biotite adamellite is grayish-white and pink, with porphyritic texture and massive structure (Figure 4A). The phenocryst is mainly composed of plagioclase, potassium feldspar, and quartz. The groundmass has the same mineral components as the phenocryst with fine particle structure, the dark minerals are mainly biotites, and the accessory minerals are mainly zircon, sphene, and apatite (Figure 4B). Potassium feldspar is strongly clayed and weakly sericitized, plagioclase has obvious zonal structure, with strong sericitization in the inner zone (Figure 4C). The biotite is subhedral-anhedral, light brown-dark brown, with strong chloritization, and opaque Fe-components are precipitated along the edges and the cleavage cracks of biotite. Some accessory minerals are encapsulated by biotite, such as zircon, apatite, and sphene (Figure 4B).

The hydromicatized granite is grayish-white and yellowish green, with porphyritic texture and massive structure (Figure 4D). It is mainly composed of feldspar, quartz, muscovite, and hydromica, and some opaque minerals are found in groundmass minerals. Quartz is anhedral and irregularly granular, which is mostly transformed from microcrystalline quartz by recrystallization (Figure 4E,F). The muscovite is subhedral-anhedral, flake-like, and has scaly, high-birefrengent aggregates, and some crystals are deformed by tectonic stress (Figure 4E). Feldspar is mainly plagioclase, which is anhedral, irregular plate-like, with strong sericitization, hydromicazation and clayzation. Some feldspar crystals have been altered completely and display feldspar pseudomorphism. Hydromicazation is a hydrothermal alteration widely developed in the mining area, which is mainly formed by the hydration of mica and feldspar. Some hydromica interweaves with sericite, and a small amount of sericite transforms into fine-scale muscovite by recrystallization.

Altered granite-type uranium ore is brownish yellow, with unequigranular texture and massive structure (Figure 4G). It is mainly composed of quartz, fluorite, pyrite, biotite, and a small amount of hematite. The ore is strongly altered by pyritization, fluoritization, silicification, and hematitization. Quartz is anhedral granular and locally distributed as vein-like in hand specimens, which may be attributed to silicic veins being interpenetrated at the post-ore stage (Figure 4G). Fluorite is violet black, mostly anhedral, and irregular granular. Intragranular cracks are widespread in the fluorite, and black, opaque Fe-components are filled along the cracks (Figure 4H). Pyrite is widely distributed in the ore, and its reflection color is bright yellow. There are biotite and microcrystalline quartz around the pyrite particles. The biotite is anhedral, scale-like, and radial-like with a yellowish green color, which is locally replaced by dark green chlorite. Pitchblende has a brownish-grey reflection color, filling around the gangue minerals in veinlet and colloid forms, and hematite is mainly distributed in mineral fissures in the form of powders (Figure 4I).

The microcrystalline quartz-type uranium ore is brownish red, has a cryptocrystalline-microcrystalline texture, and has massive structure. There are pores on the ore surface filled with

yellowish-green secondary uranium mineral (autunite); silicification and hematitization are obviously strongly developed (Figure 4J). Cross-polarized transmitted microscopy shows that the ore has a microcrystalline texture, mainly composed of microcrystalline quartz, cryptocrystalline chalcedony, and uranium minerals, as well as accessory minerals such as hematite, etc. Cryptocrystalline chalcedony transforms into microcrystalline quartz by recrystallization (Figure 4K). Uranium minerals are mainly pitchblende with brownish-grey reflection color and irregular shape. There are many microcrystalline quartz and hematite particles around the uranium minerals, of which hematite particles have brownish-red internal reflection color (Figure 4L).
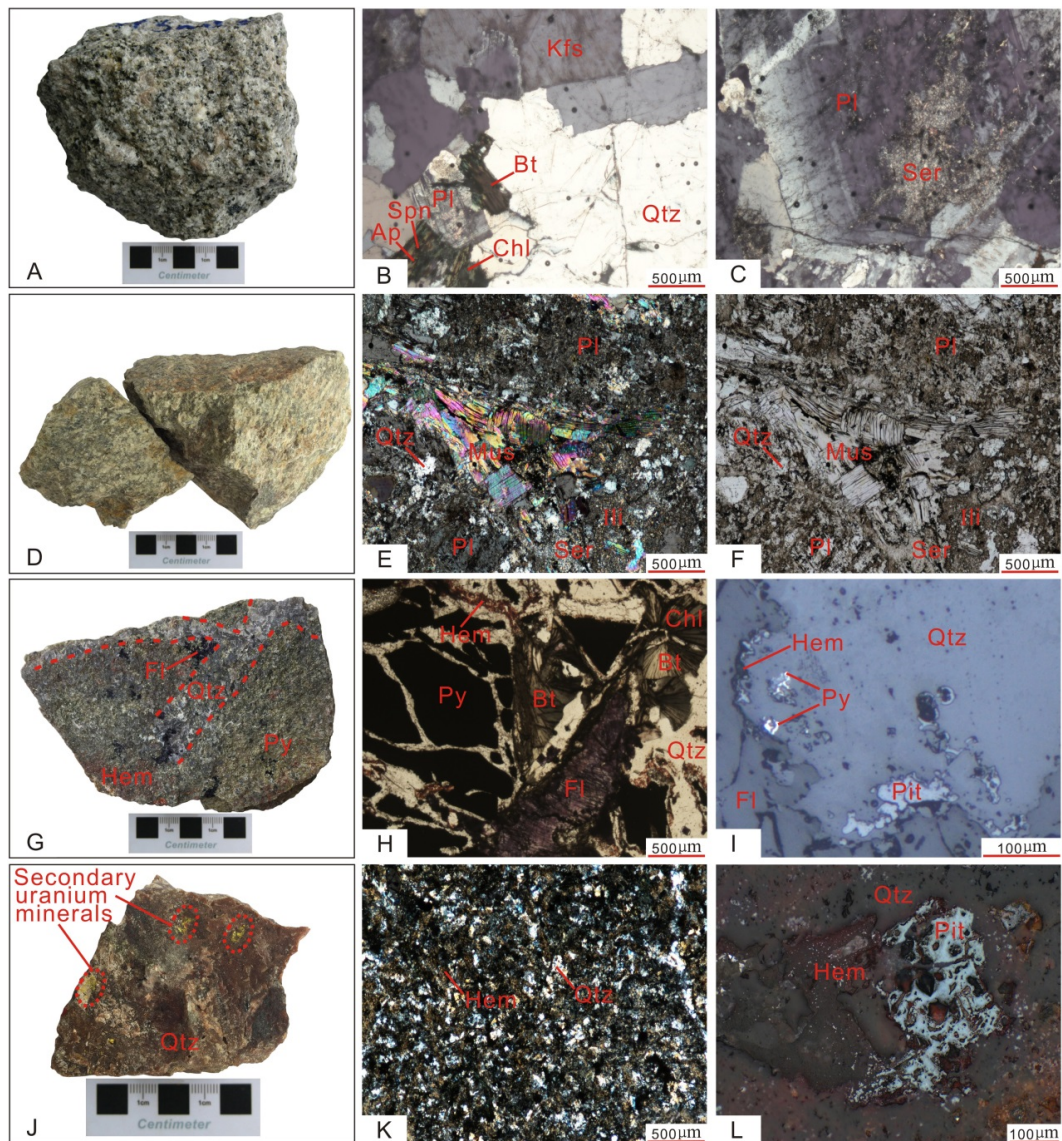
Figure 4. Representative altered rocks and petrographic characteristics in Huangsha uranium mining area. Note: Images. (**A**,**D**,**G**,**J**) are hand specimen photographs; Images. (**B**,**C**,**E**,**K**) are cross-polarized transmitted microscopy photographs; Images. (**F**,**H**) are plane-polarized transmitted microscopy photographs; Images. (**I**,**L**) are reflected microscopy photographs. Abbreviations: Pit—pitchblende; Qtz—Quartz; Bt—biotite; Ap—apatite; Spn—Sphene; Hem—hematite; Fl—Fluoritization; Kfs—potassium feldspar; Pl—plagioclase; Chl—chlorite; Py—pyrite; Ser—sericite; Ili—illite or hydromica; Mus—Muscovite.

3. Sample Characteristics and Analytical Methods

In order to understand the role of chloritization in the metallogenic process, representative chloritic granite and ore samples of different occurrences and genesis were collected. The samples' properties and location are shown in Table 1 and Figure 2A.

Table 1. Sampling locations and characters of chloritic samples from Huangsha uranium mining area.

Number of Samples	Sampling Position	Lithologic Characteristics	Alteration Information
HS52	Near the alteration zone of Egongtang uranium deposit	Medium grain granite	Hematization, chloritization, and pyritization
HS61	Far from the alteration zone of Egongtang uranium deposit	Medium-coarse grained granite	Hydromicazation, hematitization and chloritization
HS62	Egongtang uranium deposit	Uranium ore	Hematization, chloritization and silicification
HS72	Shangjiao uranium deposit	Uranium ore	Hematization, chloritization and silicification
HS74	Shangjiao uranium deposit	Uranium ore	Hematization, chloritization and silicification
HS80	Near the alteration zone of Shangjiao uranium deposit	Medium grain granite	Hydromicazation, hematitization and chloritization
HS81	Far from the alteration zone of Shangjiao uranium deposit	Medium grain granite	Hydromicazation, chloritization and kaolinization
HS86	Far from the alteration zone of Shangjiao uranium deposit	Medium-coarse grained granite	Chloritization
HS96-2	Near the alteration zone of Liangsanzhai uranium deposit	Uranium ore	Hematization, chloritization and pyritization
HS98	Near the alteration zone of Liangsanzhai uranium deposit	Medium-coarse grained granite	Hematization, chloritization and pyritization

Representative chloritic granite and ore samples collected from different occurrences and genesis were prepared into thin sections and EPMA sections. The chemical composition from the micro-area analysis of chlorites were completed in the EPMA laboratory of the National Key Laboratory of Nuclear Resources and Environment of East China University of Technology (Nanchang, China). The instruments used were a JXA-8100 Electron probe microanalyzer and an Inca Energy Spectrometer. The test conditions are as follows: the acceleration voltage is 15 kV, the probe beam is 2.0×10^{-8} A, and the electron beam spot diameter is 2 μm. The testing process was carried out according to the national standard for quantitative analysis of silicate minerals (GB/T15617-2002) [41]. In the selection of standard minerals, chlorite was used as standard sample for Mg, Fe, Al, and Si, and jadeite, potassium feldspar, apatite, rutile, chromium oxide, and rhodonite were used as standard samples of Na, K, Ca, Ti, Cr, and Mn elements, respectively.

As the electron probe cannot detect Fe^{3+}, Zheng (1983) [42] proposed that the value of Fe^{3+} can be calculated by the method of valence difference. The FeO value in EPMA data used Fe^{3+} as Fe^{2+}, and the total cation electrovalence in the molecular formula is lower than the theoretical electrovalence. Therefore, the content of Fe^{3+} can be calculated according to the principle of equilibrium of the summation of cation positive and anion negative valences of the mineral. The lining, inclusion, mixed layer structure, and complex symbiosis of minerals can lead to errors in EPMA data of chlorite. According to Foster (1962) [43], Hillier and Velde (1991) [44], Zang and Fyfe (1995) [45], the criterion of $w(Na_2O + K_2O + CaO) < 0.5\%$ is proposed as a criterion to judge whether chlorite is contaminated or not ($w < 0.5\%$ indicate that chlorite is not contaminated, $w > 0.5\%$ indicate that chlorite is contaminated). According to this criterion, inconsistent data were removed in this paper.
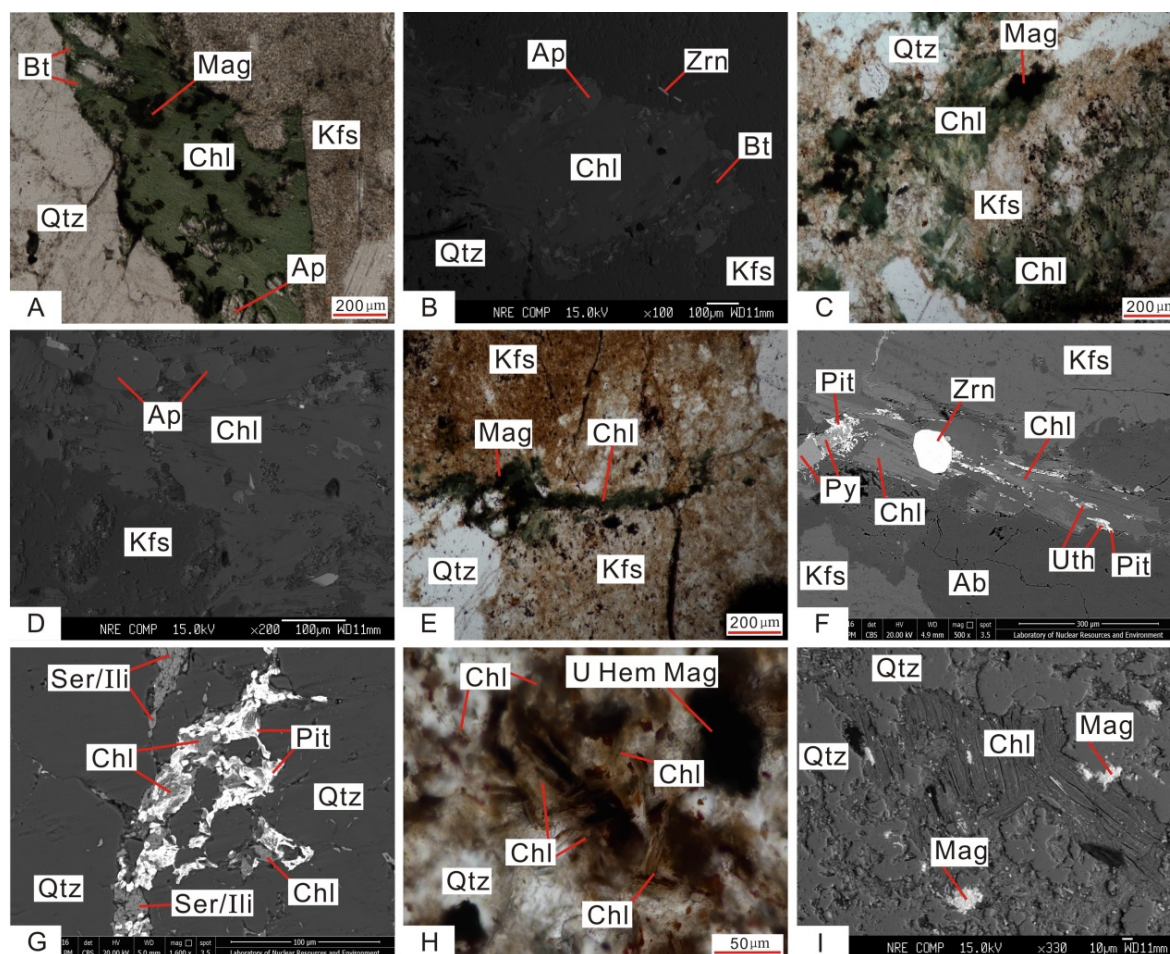
4. Chlorites Morphology

According to field investigation, hand specimens, and detailed microscopic characteristics, chlorites in Huangsha uranium mining area can be classified into five types: biotite alteration type (type-I chlorite from biotites), feldspar alteration type (type-II chlorite from the metasomatism of feldspar with Fe–Mg hydrothermal fluids), fissure filling type (type-III chlorite occurred in vein/veinlet), closely associated with uranium minerals type (type-IV uranium-associated chlorite), and transformation type from clay minerals by adsorbing Mg- and Fe-components (type-V chlorite transformed from clay minerals). Among them, type-I chlorite is the most widely distributed, with obvious polychromatism under plane-polarized transmitted microscopy, yellowish green, ink-blue, subhedral-anhedral with hypo-edge angle, and leaf-shaped. It is formed by biotite alteration at the premetallogenic stage. It often partially or completely metasomatizes biotite and retains biotite pseudomorphism. The cleavage cracks and interstices of chlorite often contain minerals such as apatite, zircon, and magnetite (Figure 5A,B). Type-II chlorite is green to brown, closely related to feldspar, usually irregularly distributed in feldspar with small and fragmented particles, and often coexists with quartz, zircon, apatite, and magnetite. It is formed by the metasomatism of feldspar with Fe–Mg hydrothermal fluids during pre-metallogenic stage (Figure 5C,D). Type-III chlorite is generally formed by vein/veinlet filling between the fissures and crystals of feldspar and quartz at the early metallogenic stage (Figure 5E). Type-IV chlorite is closely associated with pitchblende, which is vein-like and disseminated, and is often accompanied by a small amount of zircon, uranothorite, sericite or illite/hydromica, pyrite, and rare earth minerals. It is formed by filling and precipitation of ore-forming fluid at the main metallogenic stage (Figure 5F,G). Among them, zircon and chlorite are paragenetic in space, and these very small bright veinlets (pitchblende) and the slightly dark uranothorite occur in chlorite with the occurrence state of dispersive adsorption and are closely associated with pyrite and sericite (Figure 5F). Type-V chlorite is yellowish green and dark green, with no obvious pleochroism, and takes on an irregular granular structure under plane-polarized transmitted microscopy. It is similar to leaf-shaped and pinnate-shaped chlorite. It is formed by a large number of clay minerals adsorbing Mg- and Fe-components in ore-forming fluids at the main metallogenic stage and is then transformed to chlorite and biotite. A small amount of uranium minerals, hematite, and magnetite are often adsorbed around the type-V chlorite (Figure 5H,I).

5. Mineral Chemistry of Chlorite

The chemical composition of chlorites with different types were analyzed by EPMA (Table 2). The results showed that the type-I chlorite $w(SiO_2)$ ranged from 22.19% to 25.28%, with an average of 23.58%; $w(Al_2O_3)$ ranged from 16.98% to 20.74%, with an average of 19.80%; $w(FeO)$ ranged from 26.17% to 38.53%, with an average of 30.97%; $w(MgO)$ ranged from 5.29% to 13.06%, with an average of 9.52%. Type-II chlorite $w(SiO_2)$ ranged from 22.62% to 26.04%, with an average of 24.01%; $w(Al_2O_3)$ ranged from 17.12% to 20.75%, with an average of 19.41%; $w(FeO)$ ranged from 27.55% to 35.90%, with an average of 31.98%, $w(MgO)$ ranged from 6.37% to 12.75%, with an average of 9.53%. Type-III chlorite $w(SiO_2)$ ranged from 23.21% to 27.02%, with an average of 25.53%; $w(Al_2O_3)$ ranged from 18.38% to 21.09%, with an average of 19.36%; $w(FeO)$ ranged from 15.36% to 34.32%, with an average of 25.37%; $w(MgO)$ ranged from 6.17% to 21.77%, with an average of 13.52%. Type-IV chlorite $w(SiO_2)$ ranged from 24.38% to 27.86%, with an average of 26.60%; $w(Al_2O_3)$ ranged from 18.05% to 20.37%, with an average of 19.54%; $w(FeO)$ ranged from 14.73% to 32.63%, with an average of 23.30%; $w(MgO)$ ranged from 7.56% to 22.5%, with an average of 15.01%. Type-V chlorite $w(SiO_2)$ ranged from 24.46% to 29.12%, with an average of 26.01%; $w(Al_2O_3)$ ranged from 17.56% to 20.98%, with an average of 19.49%; $w(FeO)$ ranged from 29.25% to 31.01%, with an average of 30.03%; $w(MgO)$ ranged from 6.81% to 8.40%, with an average of 7.26%.

Figure 5. Morphological features of chlorites from Huangsha uranium mining area. Note: Images. A, C, E, and H are plane-polarized transmitted microscopy photographs; Images. B, D, F, G, and I are electron back scattering patterns. **A**—Chlorite with obvious polychromatism under plane-polarized transmitted microscopy, yellowish green, ink-blue, subhedral-anhedral with hypo-edge angle and leaf-shaped. **B**—The cleavage cracks and interstices of chlorite often contain minerals such as apatite, zircon and magnetite. **C,D**—Chlorite is closely related to feldspar, usually irregularly distributed in feldspar with small and fragmented particles, and often coexist with quartz, zircon, apatite and magnetite. **E**—Chlorite is generally formed by vein/veinlet filling between the fissures and crystals of feldspar and quartz. **F**—Chlorite is closely associated with pitchblende, often accompanied by a small amount of zircon and uranothorite. The very small bright veinlets (pitchblende) and the slightly dark uranothorite occur in chlorite with the occurrence state of dispersive adsorption. **G**—Chlorite is closely associated with pitchblende, often accompanied by sericite or illite/hydromica. **H**—Chlorite is yellowish green and dark green, with no obvious pleochroism and takes on an irregular granular structure under plane-polarized transmitted microscopy. **I**—Chlorite is similar to leaf-shaped and pinnate-shaped structures. Abbreviations: Pit—pitchblende; Uth—uranothorite; Qtz—Quartz; Bt—biotite; Ap—apatite; Hem—hematite; Mag—magnetite; U—uranium minerals; Zrn—zircon; Kfs—potassium feldspar; Ab—albite; Chl—chlorite; Ser—sericite; Ili—illite or hydromica.

Overall, the variation range of MgO and FeO contents in chlorite from Huangsha uranium mining area is relatively large, and there are growth–decline relationships between them, indicating that the replacement of Mg and Fe in chlorite is common. The changes of Na, K, and Ca contents (the contents of CaO, Na_2O, and K_2O are very low and almost completely migrate—most of Ca, Na, and K are lost during chloritization) indicates the degree of chloritization of the wall rock. The chemical composition is obviously different between different types of chlorite. Type-I, II, and V chlorite are relatively rich

in Fe and poor in Mg, while type-III and IV chlorite (especially type-IV chlorite, which is closely associated with uranium minerals) is characterized by the addition of Mg and the depletion of Fe, which suggests the substitutional relationship of the material composition between uranium minerals and chlorites during mineralization [5,46,47].

Table 2. Electronic microprobe analyses of chlorites from Huangsha uranium mining area.

Type	Measure Points	SiO₂	TiO₂	Al₂O₃	FeO	MnO	MgO	CaO	Na₂O	K₂O	Cr₂O₃	NiO	H₂O*	Total
I	HS52.7	23.08	0.01	20.74	29.63	0.67	11.31	0.01	0.12	0.02	-	0.02	10.73	96.67
I	HS52.13	22.45	0.02	20.62	29.82	0.62	11.77	0.07	0.11	-	0.09	-	10.68	96.91
I	HS52.14	23.5	0.04	16.98	35.69	0.58	7.53	0.07	0.12	0.01	-	-	10.18	94.86
I	HS61.2	23.25	0.11	19.41	27.98	0.32	13.06	0.08	0.04	0.05	0.03	-	10.65	95.19
I	HS86.1	24.91	0.06	19.92	27.04	0.60	10.97	0.07	0.18	0.10	0.15	-	10.72	94.80
I	HS86.10	25.09	0.03	19.56	27.98	0.44	10.37	0.03	0.13	0.12	0.10	0.07	10.66	94.81
I	HS86.14	24.16	0.05	19.43	26.53	0.39	10.11	0.07	0.13	0.05	0.03	-	10.33	91.30
I	HS86.18	25.28	-	20.39	26.17	0.55	10.99	0.03	0.15	0.11	0.09	-	10.77	94.67
I	HS96-2.17	23.48	0.06	20.59	33.96	1.31	6.75	-	0.02	-	0.07	-	10.55	96.88
I	HS98.5	22.19	0.18	19.57	38.53	1.19	5.29	0.07	0.11	-	0.18	-	10.34	97.53
I	HS98.13	22.81	0.08	20.06	34.81	1.14	7.64	-	0.04	-	0.09	0.04	10.52	97.34
I	HS98.14	22.76	0.07	20.33	33.53	1.13	8.47	0.04	0.08	0.02	0.07	-	10.57	97.08
II	HS52.19	24.75	0.13	17.12	30.13	0.42	11.69	0.21	0.01	0.04	0.18	0.04	10.58	95.31
II	HS52.20	25.93	0.11	19.98	27.55	0.30	12.75	0.06	0.06	-	0.08	0.13	11.13	98.40
II	HS61.8	24.27	0.15	20.75	28.04	0.48	12.25	0.09	-	-	0.18	0.03	10.96	97.22
II	HS61.10	26.04	0.52	19.55	27.68	0.48	11.42	0.03	0.05	0.40	0.1	-	11.00	97.30
II	HS98.3	22.62	0.21	19.16	35.71	1.17	6.37	-	0.09	-	0.21	-	10.29	95.89
II	HS98.4	22.91	0.22	20.12	32.72	1.07	8.84	0.06	0.04	0.05	0.22	0.02	10.59	96.85
II	HS98.11	23.51	0.03	19.70	34.17	1.3	8.54	-	-	-	0.03	-	10.65	97.98
II	HS98.12	23.50	0.01	20.10	33.22	1.12	8.80	-	0.02	-	0.01	0.05	10.66	97.69
II	HS98.14	23.28	0.13	17.24	35.9	0.96	6.74	0.01	0.06	0.03	0.13	-	10.14	94.79
II	HS98.16	23.32	0.07	20.33	34.63	1.18	7.94	0.03	0.08	0.03	0.07	0.05	10.69	98.69
III	HS62.6	26.30	-	18.38	16.76	0.83	20.39	0.16	0.01	0	0.07	-	11.18	95.71
III	HS62.13	26.51	0.02	19.36	16.32	0.91	21.43	0.05	0.01	0.01	0.08	0.04	11.47	96.62
III	HS62.16	27.02	-	18.62	15.36	0.89	21.77	-	0.01	-	0.09	-	11.40	96.07
III	HS62.22	26.31	-	18.62	15.85	0.81	21.32	0.10	0.09	0.01	0.01	0.01	11.26	96.02
III	HS80.7	26.59	0.02	19.58	26.20	0.51	11.81	0.09	0.13	0.05	0.11	0.03	10.98	96.47
III	HS81.7	26.20	0.06	19.89	25.15	0.47	12.86	0.07	0.05	0.06	0.06	0.01	11.01	96.19
III	HS86.17	26.37	0.05	19.81	26.57	0.47	11.72	0.05	0.20	0.07	0.10	-	10.99	96.51
III	HS86.23	25.85	0.08	21.09	26.86	0.41	10.23	-	0.07	0.05	0.08	-	10.91	95.68
III	HS96-2.16	23.21	0.07	19.95	34.14	1.52	6.17	0.10	0.13	-	0.07	-	10.38	95.94
III	HS98.8	24.19	0.06	19.32	34.32	1.11	7.67	0.08	0.04	-	0.06	0.05	10.62	97.90
III	HS98.10	24.10	0.10	18.85	34.29	0.98	7.69	0.10	0.10	0.03	0.10	-	10.54	97.09
III	HS98.15	23.73	-	18.90	32.64	1.26	9.13	-	-	-	-	0.04	10.53	96.41
IV	HS62.5	27.07	0.04	18.98	15.51	0.59	22.26	0.05	-	0.01	0.05	-	11.52	96.26
IV	HS62.14	27.86	-	19.81	14.73	0.68	22.21	0.11	0.01	0.02	0.06	-	11.73	97.96
IV	HS62.17	27.18	0.03	19.36	16.32	0.72	20.09	0.06	0.09	0.04	-	-	11.39	95.61
IV	HS62.18	26.85	0.06	19.16	15.19	0.67	22.50	0.02	0.01	0.03	0.01	-	11.52	96.20
IV	HS80.02	27.13	-	19.40	25.72	0.36	12.84	0.05	0.11	0.05	0.12	0.04	11.13	97.51
IV	HS80.03	27.09	0.02	20.29	25.14	0.37	12.77	0.01	0.14	0.03	0.1	-	11.20	97.41
IV	HS80.09	26.71	0.01	19.78	26.04	0.38	12.11	0.04	0.08	0.08	0.08	0.04	11.04	96.71
IV	HS81.04	26.61	0.07	19.83	24.82	0.49	13.39	0.09	0.08	0.08	0.15	-	11.13	96.79
IV	HS81.08	26.81	0.03	20.19	25.58	0.50	12.55	0.02	0.16	0.07	0.09	-	11.15	97.16
IV	HS81.11	26.37	0.04	20.37	26.29	0.66	12.02	0.06	0.07	0.04	0.03	0.02	11.09	97.12
IV	HS98.7	25.12	0.14	19.27	31.59	0.84	9.76	0.02	0.12	0.08	0.14	0.06	10.85	98.23
IV	HS98.9	24.38	0.14	18.05	32.63	1.00	7.56	0.06	0.19	0.12	0.14	0.06	10.35	94.88
V	HS72.04	24.46	0.20	17.56	29.25	0.62	7.68	0.12	0.05	0.05	0.01	0.04	10.02	90.20
V	HS72.09	26.02	0.22	18.35	29.37	0.57	7.18	0.09	0.03	0.09	0.09	-	10.35	92.39
V	HS72.13	24.90	0.04	19.45	30.68	0.70	6.81	0.09	0.07	0.01	0.05	-	10.35	93.19
V	HS74.01	29.12	0.31	20.15	29.50	0.59	8.40	0.10	0.06	0.10	0.05	-	11.33	99.72
V	HS74.05	26.16	0.06	20.49	30.69	0.71	6.81	0.05	0.06	-	0.05	-	10.73	95.82
V	HS74.08	26.41	0.04	20.98	31.01	0.82	6.92	0.04	0.11	-	0.13	-	10.90	97.44
V	HS74.12	25.02	0.07	19.48	29.74	0.67	7.03	0.08	0.06	0.05	0.13	0.05	10.35	92.85

Note: analytical and testing units: East China University of Technology State Key Laboratory of Nuclear Resources and Environment, "-" Represents below the detection limit, "H₂O*"—The calculated content of H₂O, I—Chlorite from biotites, II—Chlorite closely associated with feldspar, III—Chlorite occurred in vein, IV—Uranium-associated chlorite, V—Chlorite transformed from clay minerals.

Based on a large number of substitute relationships of chlorite, previous researchers proposed a complex classification and nomenclature method, i.e., the classification diagram of Fe-Si components of chlorite [1,43,48]. This method has been abolished by the International Association for the Study of Clays (AIPEA), because there is neither genetic significance nor structural information for chlorite. Tables 3 and 4 show the cation numbers and characteristic parameters of chlorites from Huangsha uranium mining area, which is calculated on the basis of 28 oxygen atoms. Based on the (Al + Q)–Mg–Fe compositional classification diagram which was proposed by Zane and Weiss (1998) [49], chlorites were classified and named in Figure 6. It shows that the chlorites in Huangsha uranium mining area are

mainly trioctahedral-chamosite, partly trioctahedral-clinochlore, and most of them belong to iron-rich chlorite. Among them, type-I type-II, and type-V chlorites are all composed of trioctahedral-chamosite; type-III and type-IV chlorites are mainly composed of trioctahedral-chamosite, and a few are composed of trioctahedral-clinochlore. This is obviously different from the Fe–Mg chlorite in unconformity-type uranium deposits in Canada (uranium deposits in the Asabaska Basin) and North Australia (Jabiluka uranium deposit) (Figure 6). Inoue (1995) [50] show that iron-rich chlorite is formed more easily in relatively acidic reduction environments, and the formation of iron-rich chlorite may be related to the boiling of the metallogenic fluid. The chlorite (especially type-IV chlorite, which is closely associated with uranium minerals) in Huangsha uranium mining area shows iron-rich potential, which indicates that the uranium deposits in this area were formed in a relatively acidic reduction environment, and the reduction environment is conducive to uranium mineralization. This is consistent with the results of Guo et al. (2012) [51] and Zhang et al. (2017) [52] on the metallogenesis of uranium deposits of North Guangdong in the Middle Nanling Range. Nutt (1989) [53] studied chlorite from the Jabiluka uranium deposit and suggested that Mg-rich chloritization was the product of alteration by a Mg-rich fluid, perhaps a brine, at high values of the fluid–rock ratio.

Table 3. Calculated cation numbers of chlorites from Huangsha uranium mining area (at standard of 28 oxygen atoms).

Type	Measure Points	Si	Al^{IV}	Al^{VI}	Ti	TFe	Fe^{2+}	Fe^{3+}	Mn	Mg	Ca	Na	K	R^{2+}
I	HS52.7	5.13	2.87	2.60	-	5.64	5.64	-	0.13	3.75	-	0.10	0.01	9.52
I	HS52.13	4.99	3.01	2.45	-	5.79	5.79	-	0.12	3.90	0.02	0.09	0.00	9.81
I	HS52.14	5.51	2.49	2.22	0.01	7.12	7.12	-	0.12	2.63	0.02	0.11	0.01	9.87
I	HS61.2	5.20	2.80	2.35	0.02	5.41	5.41	-	0.06	4.35	0.02	0.03	0.03	9.83
I	HS86.1	5.55	2.45	2.80	0.01	5.04	4.86	0.17	0.11	3.64	0.02	0.16	0.06	8.62
I	HS86.10	5.62	2.38	2.80	0.01	5.24	5.03	0.21	0.08	3.46	0.01	0.11	0.07	8.57
I	HS86.14	5.58	2.42	2.89	0.01	5.12	4.88	0.24	0.08	3.48	0.02	0.12	0.03	8.44
I	HS86.18	5.59	2.41	2.95	-	4.84	4.58	0.27	0.10	3.63	0.01	0.13	0.06	8.31
I	HS96-2.17	5.33	2.67	2.85	0.01	6.44	6.33	0.11	0.25	2.28	0.00	0.02	-	8.87
I	HS98.5	5.11	2.89	2.46	0.03	7.58	7.58	-	0.23	1.82	0.02	0.10	-	9.63
I	HS98.13	5.18	2.82	2.57	0.01	6.70	6.70	-	0.22	2.59	-	0.04	-	9.51
I	HS98.14	5.14	2.86	2.57	0.01	6.45	6.45	-	0.22	2.85	0.01	0.07	0.01	9.52
II	HS52.19	5.60	2.40	2.18	0.02	5.77	5.77	-	0.08	3.94	0.05	0.01	0.02	9.79
II	HS52.20	5.57	2.43	2.64	0.02	4.95	4.82	0.13	0.05	4.08	0.01	0.05	0.00	8.95
II	HS61.8	5.31	2.69	2.66	0.02	5.13	5.10	0.03	0.09	4.00	0.02	0.00	0.00	9.18
II	HS61.10	5.64	2.36	2.66	0.08	5.01	4.80	0.21	0.09	3.69	0.01	0.04	0.22	8.58
II	HS98.3	5.26	2.74	2.52	0.04	7.00	7.00	-	0.23	2.21	-	0.08	-	9.44
II	HS98.4	5.17	2.83	2.55	0.04	6.26	6.26	-	0.20	2.98	0.01	0.04	0.03	9.44
II	HS98.11	5.28	2.72	2.51	0.01	6.50	6.50	-	0.25	2.86	-	-	0.00	9.60
II	HS98.12	5.28	2.72	2.61	-	6.29	6.29	-	0.21	2.95	-	0.02	0.00	9.45
II	HS98.14	5.49	2.51	2.30	0.02	7.15	7.15	-	0.19	2.37	-	0.05	0.02	9.71
II	HS98.16	5.22	2.78	2.59	0.01	6.56	6.56	-	0.22	2.65	0.01	0.07	0.02	9.43
III	HS62.6	5.64	2.36	2.29	-	3.03	3.03	-	0.15	6.52	0.04	0.01	0.00	9.70
III	HS62.13	5.53	2.47	2.31	-	2.91	2.91	-	0.16	6.67	0.01	0.01	0.01	9.74
III	HS62.16	5.68	2.32	2.30	-	2.70	2.70	-	0.16	6.82	-	0.01	0.00	9.69
III	HS62.22	5.58	2.42	2.26	-	2.89	2.89	-	0.15	6.74	0.02	0.07	0.01	9.78
III	HS80.7	5.77	2.23	2.81	-	4.75	4.45	0.30	0.09	3.82	0.02	0.11	0.03	8.36
III	HS81.7	5.68	2.32	2.79	0.01	4.56	4.30	0.26	0.09	4.16	0.02	0.04	0.03	8.54
III	HS86.17	5.72	2.28	2.81	0.01	4.82	4.55	0.26	0.09	3.79	0.01	0.17	0.04	8.43
III	HS86.23	5.64	2.36	3.10	0.01	4.90	4.49	0.41	0.08	3.33	-	0.06	0.03	7.89
III	HS96-2.16	5.35	2.65	2.79	0.01	6.58	6.51	0.07	0.30	2.12	0.02	0.12	0.00	8.93
III	HS98.8	5.46	2.54	2.60	0.01	6.48	6.43	0.04	0.21	2.58	0.02	0.04	0.00	9.23
III	HS98.10	5.48	2.52	2.54	0.02	6.52	6.51	0.02	0.19	2.61	0.02	0.09	0.02	9.30
III	HS98.15	5.40	2.60	2.47	-	6.26	6.26	-	0.24	3.10	-	-	-	9.60
IV	HS62.5	5.63	2.37	2.28	0.01	2.73	2.73	-	0.10	6.90	0.01	-	0.01	9.73
IV	HS62.14	5.69	2.31	2.46	-	2.51	2.43	0.08	0.12	6.76	0.02	0.01	0.01	9.31
IV	HS62.17	5.71	2.29	2.51	-	2.87	2.76	0.10	0.13	6.29	0.01	0.07	0.02	9.18
IV	HS62.18	5.58	2.42	2.28	0.01	2.70	2.70	-	0.12	6.96	-	0.01	0.02	9.78
IV	HS80.02	5.81	2.19	2.74	-	4.61	4.32	0.29	0.07	4.10	0.01	0.09	0.03	8.48
IV	HS80.03	5.76	2.24	2.88	-	4.47	4.13	0.34	0.07	4.05	-	0.12	0.02	8.25
IV	HS80.09	5.77	2.23	2.83	-	4.70	4.39	0.32	0.07	3.90	0.01	0.07	0.04	8.35
IV	HS81.04	5.70	2.30	2.74	0.01	4.45	4.20	0.25	0.09	4.28	0.02	0.07	0.04	8.57
IV	HS81.08	5.73	2.27	2.84	-	4.57	4.28	0.29	0.09	4.00	-	0.13	0.04	8.36
IV	HS81.11	5.67	2.33	2.86	0.01	4.73	4.44	0.29	0.12	3.85	0.01	0.06	0.02	8.41
IV	HS98.7	5.54	2.46	2.57	0.02	5.83	5.76	0.07	0.16	3.21	-	0.10	0.05	9.13
IV	HS98.9	5.63	2.37	2.56	0.02	6.30	6.21	0.09	0.20	2.60	0.01	0.17	0.07	9.01

Table 3. *Cont.*

Type	Measure Points	Si	Al^{IV}	Al^{VI}	Ti	TFe	Fe^{2+}	Fe^{3+}	Mn	Mg	Ca	Na	K	R^{2+}
V	HS72.04	5.82	2.18	2.77	0.04	5.82	5.47	0.35	0.12	2.72	0.03	0.05	0.03	8.31
V	HS72.09	5.96	2.04	2.98	0.04	5.63	5.08	0.55	0.11	2.45	0.02	0.03	0.05	7.64
V	HS72.13	5.72	2.28	3.03	0.01	5.90	5.48	0.41	0.14	2.33	0.02	0.06	0.01	7.95
V	HS74.01	6.08	1.92	3.11	0.05	5.15	4.46	0.69	0.10	2.61	0.02	0.05	0.05	7.18
V	HS74.05	5.79	2.21	3.19	0.01	5.68	5.14	0.55	0.13	2.25	0.01	0.05	-	7.52
V	HS74.08	5.75	2.25	3.20	0.01	5.65	5.13	0.52	0.15	2.25	0.01	0.09	-	7.53
V	HS74.12	5.74	2.26	3.06	0.01	5.71	5.26	0.45	0.13	2.41	0.02	0.05	0.03	7.79

Note: R^2 = $n(Fe^{2+})$ + $n(Mn)$ + $n(Mg)$ + $n(Ca)$, I—Chlorite from biotites, II—Chlorite closely associated with feldspar, III—Chlorite occurred in vein, IV—Uranium-associated chlorite, V—Chlorite transformed from clay minerals.

Table 4. Characteristic parameters of chlorites from Huangsha uranium mining area (at standard of 28 oxygen atoms).

Type	Measure Points	n(Fe)/n(Fe + Mg)	n(Mg)/n(Fe + Mg)	n(Al)/n(Al + Fe + Mg)	d_{001}/0.1 nm	t/°C	a_3	a_6	lgK_1	lgK_2	lg(fO_2)	lg(fS_2)
I	HS52.7	0.60	0.40	0.37	14.12	262.3	9.91	−184.37	0.10	-	-	-
I	HS52.13	0.60	0.40	0.36	14.11	271.8	9.63	−193.15	0.11	-	-	-
I	HS52.14	0.73	0.27	0.33	14.12	255.6	10.11	−178.30	0.24	-	-	-
I	HS61.2	0.55	0.45	0.35	14.12	256.1	10.10	−178.76	0.07	-	-	-
I	HS86.1	0.58	0.42	0.38	14.15	230.5	10.90	−157.34	0.06	0.06	−43.6	−2.3
I	HS86.10	0.60	0.40	0.37	14.15	228.3	10.98	−155.62	0.07	0.08	−43.6	−2.5
I	HS86.14	0.60	0.40	0.38	14.15	229.0	10.95	−156.13	0.06	0.08	−43.2	−2.2
I	HS86.18	0.57	0.43	0.39	14.15	224.9	11.09	−153.01	0.05	0.08	−43.5	−2.8
I	HS96-2.17	0.74	0.26	0.39	14.12	258.0	10.04	−180.42	0.21	0.09	−41.6	−2.1
I	HS98.5	0.81	0.19	0.36	14.10	283.0	9.31	−204.06	0.43	-	-	-
I	HS98.13	0.72	0.28	0.37	14.11	270.2	9.68	−191.71	0.24	-	-	-
I	HS98.14	0.69	0.31	0.37	14.11	270.1	9.68	−191.57	0.20	-	-	-
II	HS52.19	0.59	0.41	0.32	14.14	236.7	10.70	−162.25	0.08	-	-	-
II	HS52.20	0.55	0.45	0.36	14.15	228.7	10.96	−155.95	0.05	0.04	−44.3	−2.8
II	HS61.8	0.56	0.44	0.37	14.13	246.6	10.39	−170.50	0.07	0.01	−44.9	−1.1
II	HS61.10	0.58	0.42	0.37	14.15	224.5	11.10	−152.70	0.05	0.07	−44.0	−3.1
II	HS98.3	0.76	0.24	0.36	14.11	268.7	9.72	−190.28	0.30	-	-	-
II	HS98.4	0.68	0.32	0.37	14.11	266.2	9.80	−187.92	0.17	-	-	-
II	HS98.11	0.69	0.31	0.36	14.12	262.5	9.91	−184.51	0.19	-	-	-
II	HS98.12	0.68	0.32	0.37	14.12	260.5	9.96	−182.71	0.17	-	-	-
II	HS98.14	0.75	0.25	0.34	14.12	256.9	10.07	−179.44	0.27	-	-	-
II	HS98.16	0.71	0.29	0.37	14.11	266.7	9.78	−188.38	0.22	-	-	-
III	HS62.6	0.32	0.68	0.33	14.17	206.9	11.70	−139.91	-	-	-	-
III	HS62.13	0.30	0.70	0.33	14.17	211.7	11.54	−143.28	-	-	-	-
III	HS62.16	0.28	0.72	0.33	14.18	201.1	11.91	−135.96	-	-	-	-
III	HS62.22	0.30	0.70	0.33	14.17	208.7	11.64	−141.14	-	-	-	-
III	HS80.7	0.55	0.45	0.37	14.17	213.5	11.47	−144.60	0.04	0.08	−44.5	−4.6
III	HS81.7	0.52	0.48	0.37	14.16	217.3	11.34	−147.31	0.03	0.05	−44.4	−4.1
III	HS86.17	0.56	0.44	0.37	14.16	217.7	11.33	−147.61	0.04	0.07	−44.3	−4.0
III	HS86.23	0.60	0.40	0.40	14.16	221.6	11.20	−150.50	0.05	0.12	−43.1	−2.9
III	HS96-2.16	0.76	0.24	0.38	14.12	258.4	10.03	−180.79	0.24	0.06	−42.4	−1.7
III	HS98.8	0.72	0.28	0.36	14.13	251.4	10.24	−174.63	0.19	0.03	−44.0	−0.1
III	HS98.10	0.71	0.29	0.36	14.13	250.9	10.26	−174.21	0.20	0.01	−45.8	−1.2
III	HS98.15	0.67	0.33	0.35	14.13	253.3	10.18	−176.28	0.15	-	-	-
IV	HS62.5	0.28	0.72	0.33	14.17	204.4	11.79	−138.19	-	-	-	-
IV	HS62.14	0.27	0.73	0.34	14.18	198.1	12.02	−133.97	-	-	−48.0	−7.9
IV	HS62.17	0.31	0.69	0.34	14.18	200.2	11.94	−135.41	-	-	−47.5	−7.4
IV	HS62.18	0.28	0.72	0.33	14.17	207.1	11.70	−140.08	-	-	-	-
IV	HS80.02	0.53	0.47	0.36	14.17	209.7	11.60	−141.90	0.03	0.06	−45.1	−5.3
IV	HS80.03	0.52	0.48	0.38	14.17	210.9	11.56	−142.72	0.03	0.07	−44.6	−4.9
IV	HS80.09	0.55	0.45	0.37	14.17	213.1	11.49	−144.30	0.03	0.08	−44.5	−4.6
IV	HS81.04	0.51	0.49	0.37	14.16	214.8	11.43	−145.53	0.03	0.05	−44.7	−4.5
IV	HS81.08	0.53	0.47	0.37	14.16	214.3	11.45	−145.15	0.03	0.06	−44.5	−4.5
IV	HS81.11	0.55	0.45	0.38	14.16	219.3	11.28	−148.77	0.04	0.07	−44.0	−3.7
IV	HS98.7	0.64	0.36	0.36	14.14	239.9	10.60	−164.88	0.11	0.04	−44.4	−1.7
IV	HS98.9	0.71	0.29	0.36	14.14	239.4	10.62	−164.46	0.17	0.07	−44.0	−1.5
V	HS72.04	0.68	0.32	0.37	14.16	221.1	11.21	−150.15	0.10	0.20	−43.6	−3.3
V	HS72.09	0.70	0.30	0.38	14.17	208.6	11.64	−141.08	0.08	0.31	−44.2	−5.0
V	HS72.13	0.72	0.28	0.39	14.15	226.7	11.03	−154.37	0.12	0.27	−42.7	−2.2
V	HS74.01	0.66	0.34	0.39	14.18	195.7	12.10	−132.41	0.04	0.27	−45.3	−6.8
V	HS74.05	0.72	0.28	0.41	14.16	219.3	11.28	−148.77	0.09	0.31	−43.0	−3.2
V	HS74.08	0.72	0.28	0.41	14.16	221.3	11.21	−150.26	0.09	0.30	−42.8	−2.9
V	HS74.12	0.70	0.30	0.40	14.16	223.1	11.15	−151.63	0.10	0.27	−42.9	−2.7

Note: I—Chlorite from biotites, II—Chlorite closely associated with feldspar, III—Chlorite occurred in vein, IV—Uranium-associated chlorite, V—Chlorite transformed from clay minerals; a_3—The third end-member component activity, a_6—The sixth end-member component activity, K_1—The first equilibrium constant, K_2—The second equilibrium constant, lg(fO_2)—Oxygen fugacity, lg(fS_2)—Sulfur fugacity, lg(fO_2) = 4(lga_6 − lga_3 − lgK_1), lg(fS_2) = 1/7[4lg(fO_2) − lga_3 − lgK_2], lgK_1 = 21.77e − 0.003t, lgK_2 = 0.1368t − 0.002t^2 − 82.615, t—Temperature.
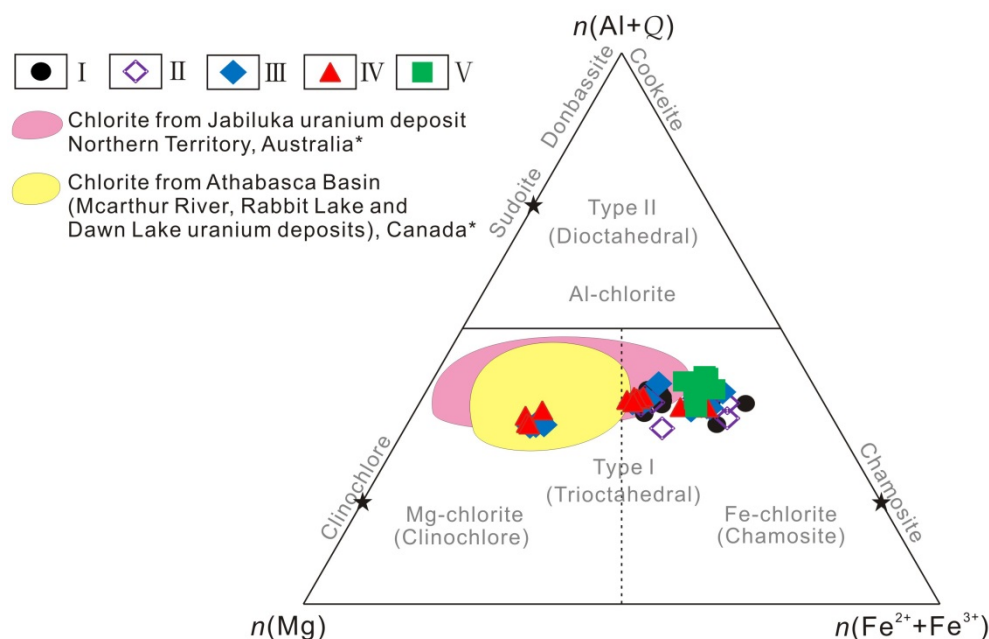
Figure 6. (Al + Q)–Mg–Fe compositional classification diagram of chlorite in Huangsha uranium mining area (According to Zane and Weiss (1998) [49]). Note: $Q = 12 - \Sigma(R^{2+} + R^{3+} + R^{4+})^{VI}$, represents structure vacancies. Black stars represent end-members: clinochlore, chamosite, and sudoite. Type I chlorites are mostly Mg-chlorites or Fe-chlorites depending on the dominant cation; Type II chlorites are mostly Al-chlorites. I—Chlorite from biotites, II—Chlorite closely associated with feldspar, III—Chlorite occurring in vein, IV—Uranium-associated chlorite, V—Chlorite transformed from clay minerals, *Data from [53–55].

6. Structural Characteristics of Chlorite

The structural formula of chlorite is $(R^{2+}_\mu, R^{3+}_y, Q_z)^{VI}(Si_{4-x} Al_x)^{IV}O_{10+w}(OH)_{8-w}$, in which IV and VI represent four-coordinate and six-coordinate centers, respectively; R^{2+} represents Mg^{2+}, Fe^{2+}, Mn^{2+}, Zn^{2+}, Ni^{2+}, etc; R^{3+} represents Al^{3+}, Fe^{3+}, Cr^{3+}, etc.; Q represents structure vacancies, $\mu + y + z = 6$, $z = (y - w - x)/2$, w is usually equal to 0 or very small [2,56]. Chlorite formed at different temperatures has different ion substitution relationships and space occupying capacity, which is also the basis for chlorite to be used as a geothermometer. Therefore, the structural characteristics of chlorite are often explained by the correlation between the main cations of chlorite.

6.1. Discrimination of the Original Rock Types of Chlorite

The diagram of the $n(Mg)/n(Fe + Mg) - n(Al)/n(Al + Mg + Fe)$ relationship proposed by Laird (1988) [57] has been widely used to distinguish the relationship between chlorite and its parent rock. Generally, chlorite formed by alteration of argillite is more than 0.35 in $n(Al)/n(Al + Mg + Fe)$, while chlorite transformed from mafic rock is less than 0.35 in $n(Al)/n(Al + Mg + Fe)$. Table 3 shows that the $n(Al)/n(Al + Mg + Fe)$ values of chlorites of various types from Huangsha uranium mining area range from 0.32 to 0.41, with an average of 0.36. Most of them are more than 0.35, and only a small number of them are less than 0.35. This indicates that different types of chlorite are derived from argillite in the mining area, and a small number of them may be affected by mantle fluids (rich in ferromagnesium), resulting in $n(Al)/n(Al + Mg + Fe)$ value less than 0.35, which coincides with the intrusion of a large number of basic dikes in Huangsha uranium mining area. The diagram of the $n(Mg)/n(Fe + Mg) - n(Al)/n(Al + Mg + Fe)$ relationship of chlorite shows a weak negative correlation (Figure 7A) and its linear equation is $n(Al)/n(Al + Mg + Fe) = -0.0823n(Mg)/n(Fe + Mg) + 0.3039$. The ratio, diagram, and equation reflect that the different types of chlorite are derived from argillite,

which is consistent with the results of Sun Tao et al. (2005) [58] on the origin of Mesozoic granite from argillite in the Middle-East Nanling Range.

6.2. Correlation of Main Cations in Chlorites

The substitution relationship between tetrahedral and octahedral positions of chlorite is usually analyzed by using $n(Al^{IV})$ and $n(Al^{VI})$ values and the relationship diagrams between $n(Fe + Al^{IV})$ and $n(Mg)$ of chlorite. The study of Xie et al. (1997) [59] shows that the ratio of $n(Al^{IV})$ to $n(Al^{VI})$ has a linear relationship of nearly 1:1 (correlation coefficient is 0.95) when the ionic substitution of the tetrahedral position is completely tschermakite-type. The $n(Al^{IV})$ value of chlorite in Huangsha uranium mining area ranges from 1.92 to 3.01, the $n(Al^{VI})$ value ranges from 2.18 to 3.20, and the value of $n(Al^{IV})/n(Al^{VI})$ ranges from 0.62 to 1.23, with a wide fluctuation range. The diagram of the $n(Al^{IV}) - n(Al^{VI})$ relationship of chlorite shows a weak negative correlation (Figure 7B) and its linear equation is $n(Al^{IV}) = -0.5048n(Al^{VI}) + 3.8952$. Therefore, the tetrahedral position of chlorite in Huangsha uranium mining area is not a purely tschermakite-type substitution. The charge generated by the replacement of Si^{4+} by Al^{IV} needs to be supplemented by the replacement of Fe or Mg by Al^{VI} in order to achieve charge balance [60]. The variation of $n(Al^{IV})/n(Al^{VI})$ (from 0.62 to 1.23, with a wide fluctuation range) also indicates that the low Fe^{3+} content of chlorite of any type may be due to the replacement of Fe or Mg by Al^{VI}.

The $n(Al^{VI} +Fe) - n(Mg)$ relationship diagram can indicate the substitution relationship of the octahedral position of chlorite [59]. From Figure 7C, it can be seen that the projection points of chlorite show a good linear negative correlation, and its linear equation is $n(Al^{VI} + Fe) = 0.9282n(Mg) + 11.344$, which indicates that the octahedral position of chlorite is mainly occupied by three elements; Al^{VI}, Fe, and Mg, and that both Al^{VI} and Fe can replace Mg in this position.

The study of Xie et al. (1997) [59] shows that the diagrams of the relationship between the main cations and magnesium can reflect the alteration process of the original rock. There is a good linear relationship between the main cations and magnesium ions on the condition that chlorite is formed by hydrothermal alteration. The diagrams of the relationship between the main cations and magnesium of chlorite in Huangsha uranium mining area (Figure 7D–G), $n(Mg) - n(Fe)$ (Figure 7D), shows a significant negative correlation and good linear relationship, and its linear equation is $n(Fe)= -0.8385\,n(Mg) + 8.3577$; $n(Mg) - n(Al^{VI})$ (Figure 5E) shows a weak negative correlation, and the linear equation is $n(Al^{VI}) = -0.0897n(Mg) + 2.9865$, while there is no linear relationship between $n(Mg) - n(Si)$(Figure 7F) and $n(Mg) - n(Al^{IV})$(Figure 7G). This suggests that chlorite in Huangsha uranium mining area is the product of multiple stages of hydrothermal action.

The diagrams of the relationship between $n(Al^{IV}) - n(Mg)/n(Fe + Mg)$ and $n(Al^{IV}) - n(Fe)/n(Fe + Mg)$ in Huangsha uranium mining area are shown in Figure 7H,I. Among them, the relationship diagram of $n(Al^{IV})$–$n(Mg)/n(Fe + Mg)$ of chlorites (Figure 7H) shows a weak negative correlation, and the linear equation is $n(Al^{IV}) = -0.4726n(Mg)/n(Fe + Mg) + 2.652$. The relationship diagram of $n(Al^{IV}) - n(Fe)/n(Fe + Mg)$ of chlorites (Figure 7I) shows a weak positive correlation, and the linear equation is $n(Al^{IV}) = 0.4726n(Fe)/n(Fe + Mg) + 2.1795$. These suggest that with the replacement of Si by Al^{IV} in the tetrahedral position, Mg is also replaced by Fe in the octahedral position, which makes the content of Fe increase and the content of Mg decrease. Owing to the process of replacement of Mg by Fe, the internal structure of chlorite is changed, which promotes the replacement of Si by Al^{IV} [59].
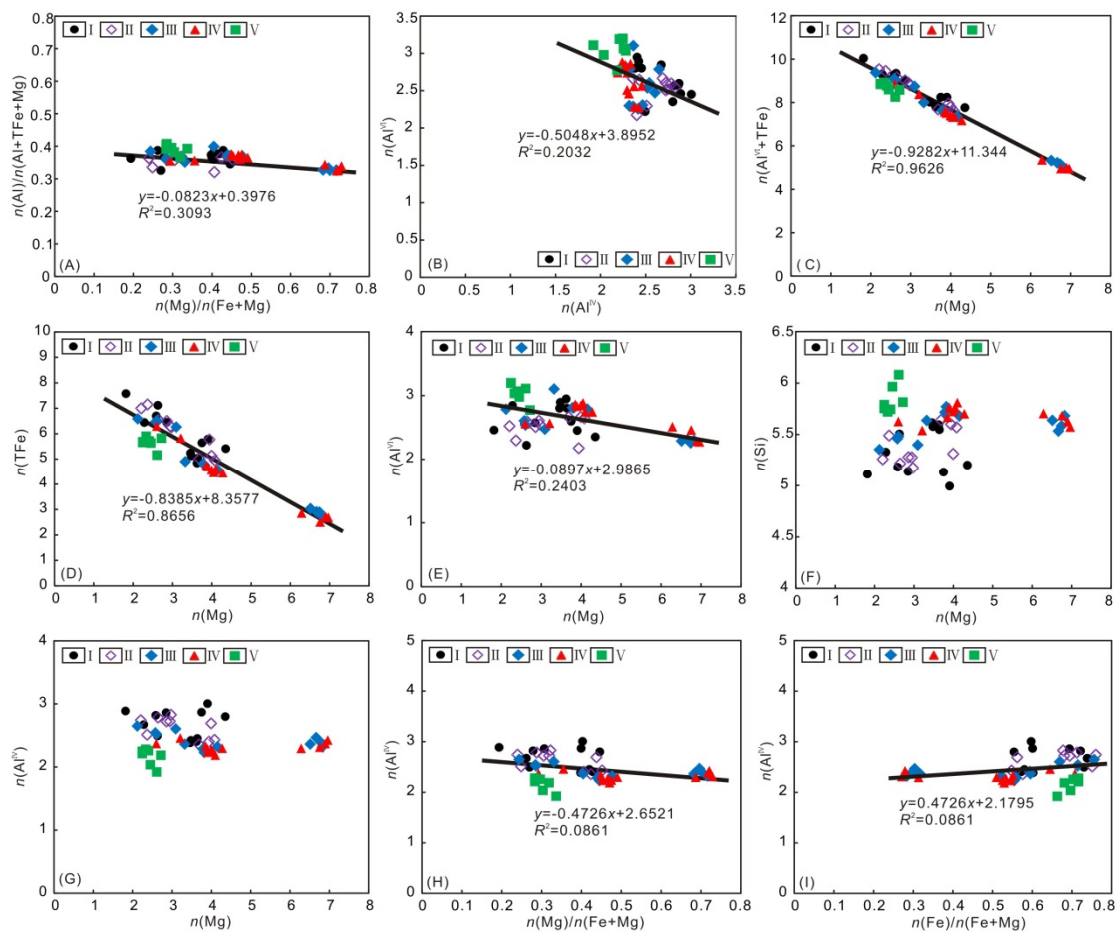
Figure 7. Graphic diagram of main cation relations of chlorites in Huangsha uranium mining area. **A**—The diagram of the $n(Mg)/n(Fe + Mg) - n(Al)/n(Al + Mg + Fe)$ relationship of chlorite. **B**—The diagram of the $n(Al^{IV}) - n(Al^{VI})$ relationship of chlorite. **C**—The diagram of the $n(Al^{VI} + Fe) - n(Mg)$ relationship of chlorite. **D**—The diagram of the $n(Mg) - n(Fe)$ relationship of chlorite. **E**—The diagram of the $n(Mg) - n(Al^{VI})$ relationship of chlorite. **F**—The diagram of the $n(Mg) - n(Si)$ relationship of chlorite. **G**—The diagram of the $n(Mg) - n(Al^{IV})$ relationship of chlorite. H—The diagram of the $n(Al^{IV}) - n(Mg)/n(Fe + Mg)$ relationship of chlorite. **I**—The diagram of the $n(Al^{IV}) - n(Fe)/n(Fe + Mg)$ of chlorite. I—Chlorite from biotites, II—Chlorite closely associated with feldspar, III—Chlorite occurring in veins, IV—Uranium-associated chlorite, V—Chlorite transformed from clay minerals.

7. Discussion

7.1. Formation Temperature of Chlorites

The relationship between the formation temperature, the structure, chemical composition, and polymorphism of chlorite has been deeply studied and widely recognized [9,19,20]. Rause-Colom et al. (1991) [19] studied the linear relationship between chlorite composition and d_{001}, and proposed the corresponding formula, modified by Nieto (1997) [20], as $d_{001}/0.1nm = 14.339 - 0.115n(Al^{IV}) - 0.0201n(Fe^{2+})$. Based on this formula, the value of interplanar spacing d_{001} is calculated in this paper. The formation temperature of chlorite is calculated according to the equation $t/°C = [14.379 - (d_{001}/0.1nm)]/0.001$, which was proposed by Battaglia et al. (1999) [11]. The formation temperature of chlorites in Huangsha uranium mining area (Table 3 and Figure 8A) ranges from 195.7 °C to 283.0 °C, with an average value of 233.2 °C. Among the chlorite types, the formation temperature of type-I chlorite is the highest, ranging from 224.9 °C to 283.0 °C, with an average value of 253.3 °C; type-II chlorite ranges from 224.5 °C to 268.7 °C, with an average value of 251.8 °C; type-III chlorite ranges

from 201.1 °C to 258.4 °C, with an average value of 226.0 °C; type-IV chlorite is the lowest, ranging from 198.1 °C to 239.9 °C, with an average value of 214.3 °C; type-V chlorite ranges from 195.7 °C to 226.7 °C, with an average value of 216.5 °C. The formation temperatures of various types of chlorite suggest the chlorite from premetallogenic stage (type-I and type-II chlorite, with an average value of 252.6 °C) → early metallogenic stage (type-III chlorite, with a value of 226.0 °C) → main metallogenic stage (type-IV and type-V chlorite, with an average value of 215.4 °C) decreases continuously, which belongs to medium-low temperature hydrothermal alteration. Guo et al. (2010) [61] and Guo et al. (2012) [51] used fluid inclusion thermometry and a chlorite geothermometer to research the metallogenic temperature of No.302 uranium deposit (a well-known granite-type uranium deposit, located about 150 km north-west of Huangsha uranium mining area), respectively. The results of these two methods show very similar metallogenic temperature, about 210 °C. The temperature of ore-forming fluids decreases continuously from the early metallogenic stage to the main metallogenic stage. The temperature measurement results of Huangsha uranium mining area by chlorite geothermometer are very close to those of No.302 uranium deposit.

7.2. Formation Oxygen Fugacity and Sulfur Fugacity of Chlorites

The formation oxygen fugacity [$\lg(fO_2/10^{-5}$ Pa)] and sulfur fugacity [$\lg(fS_2/10^{-5}$ Pa)] of chlorite can effectively indicate the physicochemical formation conditions. Walshe (1986) [17], Bryndzia and Scott (1987) [9] calculated the formation oxygen fugacity, sulfur fugacity, temperature, and pressure of chlorite according to its composition. In this paper, the calculation method proposed by Walshe (1986) [17] is used to calculate the formation oxygen fugacity and sulfur fugacity of chlorite by using the functional relationship between reaction equilibrium constant and temperature, which is fitted by Zhang et al. (2014) [62]. The calculation process and method refer to Li et al. (2017) [47] and Zhang et al. (2014) [62]. The calculated results (Table 3, Figure 8B,C) show that the $\lg(fO_2/10^{-5}$ Pa) value of chlorite ranges from −48.0 to −41.7, with an average value of −44.2, and the $\lg(fS_2/10^{-5}$ Pa) value of chlorite ranges from −7.9 to −0.1, with an average value of −3.4, which suggests an environment of low oxygen fugacity. Figure 9A and relatively high sulfur fugacity $\lg(fS_2/10^{-5}$ Pa) − *T* projective points of all types of chlorite are above the Bn + Py − Cp buffer line, suggesting an environment of high sulfur fugacity (Figure 9B). The oxygen fugacity [$\lg(fO_2/10^{-5}$ Pa)] and sulfur fugacity [$\lg(fS_2/10^{-5}$ Pa)] of type-I chlorite range from −43.7 to −41.7 and −2.8 to −2.1, with average values of −43.1 and −2.4, respectively. Type-II chlorite ranges from −45.0 to −44.0 and −3.1 to −1.2, with average values of −44.4 and −2.4, respectively. Type-III chlorite ranges from −45.8 to −42.4 and −4.6 to −0.1, with average values of −44.1 and −2.7, respectively. Type-IV chlorite ranges from −48.0 to −44.0 and −7.9 to −1.7, with average values of −45.1 and −4.9, respectively. Type-V chlorite ranes from −45.3 to −42.7 and −6.9 to −2.2, with average values of −43.5 and −3.7, respectively. The oxygen fugacity and sulfur fugacity of various types of chlorite generally decrease in the order of premetallogenic stage (type-I and type-II chlorite, the average values of oxygen fugacity and sulfur fugacity are −43.8 and −2.4, respectively) → early metallogenic stage (type-III chlorite, with a values of oxygen fugacity and sulfur fugacity −44.1 and −2.7, respectively) →main metallogenic stage (type-IV and type-V chlorite, the average values of oxygen fugacity and sulfur fugacity are −44.3 and −4.3, respectively), which suggests the hydrothermal metasomatic alteration process of Huangsha uranium mining area is gradually evolving towards low oxygen fugacity and relatively high sulfur fugacity, that is, hydrothermal fluids are becoming more and more reductive. Ling (2011) [63] reviewed the oxygen fugacity characteristics of granite-type uranium deposits in South China. It is considered that the original rocks were derived from argillite, and then formed sedimentary rocks enriched with U^{4+} and Fe^{2+} (e.g., pyrite) in the reductive environment. The oxygen fugacity of uranium-bearing granite formed by these sedimentary rocks melts partially, which is lower than that of uranium-barren granite (uranium-bearing granite is below the NiO–Ni buffer line, uranium-barren granite is between the Hm–Mt and NiO–Ni buffer line). These characteristics are consistent with the results of using chlorite to research the metallogenic environment of Huangsha uranium mining area. The distribution range

of oxygen fugacity and sulfur fugacity of chlorite in unconformity-type uranium deposits (Asabaska Basin and Jabiluka) are wider than those in Huangsha uranium deposit (Figure 9A,B), which may be attributed to the chlorite in unconformity-type uranium deposit often metasomatizing minerals such as biotite, garnet, amphibole, cordierite, and tourmaline. Retrograde alteration and epigenetic alteration also developed obvious chloritization, silicification, and carbonation (such as magnesite mineralization and dolomitization) [53,54,64]. Compared with the granite-type uranium deposits, their metamorphism is more intense and the formation environment is more complex.
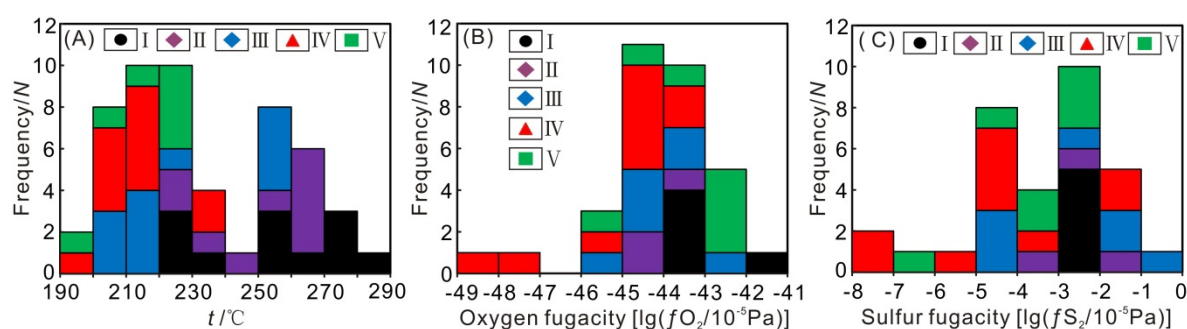
Figure 8. Histogram of formation temperatures, oxygen fugacity, and sulfur fugacity for chlorites from Huangsha uranium mining area. **A**—The formation temperatures frequency distribution histogram of chlorites. **B**—The formation oxygen fugacity frequency distribution histogram of chlorites. **C**—The formation sulfur fugacity frequency distribution histogram of chlorites. I—Chlorite from biotites, II—Chlorite closely associated with feldspar, III—Chlorite occurring in veins, IV—Uranium-associated chlorite, V—Chlorite transformed from clay minerals.
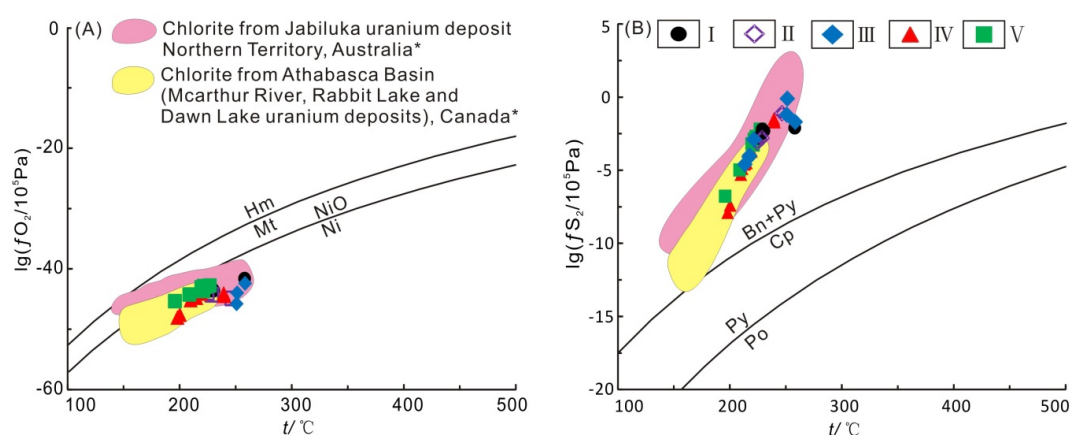
Figure 9. $\lg(fO_2/10^{-5}$ Pa) values of oxygen fugacity and $\lg(fS_2/10^{-5}$ Pa) values of sulfur fugacity buffers as functions of temperature. Base maps are according to Eugster and Wones, (1962) [65]; Ling, (2011) [63]; Liu et al. (2016) [66]. **A**—The diagram of the oxygen fugacity buffers as functions of temperature. **B**—The diagram of sulfur fugacity buffers as functions of temperature. Abbreviations: Hm—hematit; Mt—magnetit; Bn—Bornite; Py—pyrite; Cp—chalcopyrite; Po—pyrrhotite; Ni—nickel; NiO—nickel oxide. I—Chlorite from biotites, II—Chlorite closely associated with feldspar, III—Chlorite occurred in vein, IV—Uranium-associated chlorite, V—Chlorite transformed from clay minerals, *Data from [53–55].

7.3. Formation Mechanisms of Chlorites

The formation process of chlorite is a water–rock reaction process controlled by reaction kinetics, which is restricted by temperature, pressure, water/rock ratio, fluid, and petrochemical composition [5]. The chloritization of Huangsha uranium mining area is widespread. At the premetallogenic stage, biotite and feldspar are often partially or completely metasomatized by hydrothermal fluids (contains Fe and Mg), and form chlorite with the characteristics of pseudomorphism (Figure 5A,B) and

metasomatic alteration structure (Figure 5C,D). At the early metallogenic stage, hydrothermal fluid fills in the interstices and fissures of feldspar, quartz, and other minerals to form vein/veinlet chlorite (Figure 5E). At the main metallogenic stage, chlorite is closely associated with pitchblende, zircon, apatite, hematite, and magnetite (Figure 5F–I). The chemical composition of chlorites in Huangsha uranium mining area shows that the chlorite belongs to iron-rich chlorite, which indicates that the fluids are rich in Fe or that the fluids extract Fe-components from the wallrocks during their migration. The studies of Inoue (1995) [50] suggest that the relatively acidic reduction environment is favorable for the formation of iron-rich chlorite in vein-type deposits during hydrothermal alteration. According to Liu and Cao (1987) [67], the migration medium of Fe is reductive. In conclusion, various types of chlorite in Huangsha uranium mining area are formed in a relatively acidic reducing environment.

Zhang et al. (2007) [5], Li et al. (2016) [46], and Li et al. (2017) [47] suggest that the formation of chlorite can be classified into two mechanisms: dissolution–precipitation and dissolution–migration–precipitation. Based on the study of mineralogical characteristics of chlorite in Huangsha uranium mining area by electron microscope and EPMA, combined with the results of the formation environment of chlorite, it is considered that the formation mechanism of type-I chlorite (chlorite from biotite) and type-II chlorite (chlorite closely associated with feldspar) is the dissolution–precipitation mechanism, which is mainly manifested by hydrothermal fluid metasomatizing biotite and feldspar, and transformation into chlorite, retaining biotite pseudomorphism and metasomatic alteration structure, respectively. The formation mechanism of type-III chlorite (chlorite occurred in vein), type-IV chlorite (uranium-associated chlorite), and type-V chlorite (chlorite transformed from clay minerals) is the dissolution–migration–precipitation mechanism. The hydrothermal fluid dissolves some Fe- and Mg-rich minerals and forms Fe- and Mg-rich hydrothermal fluids. They precipitate and crystallize in other minerals' fissures through migration, or Fe- and Mg-components are adsorbed by a large number of clay minerals and then transformed to chlorite and biotite.

7.4. Relationship between Chlorites and Uranium Mineralization

Chloritization is one of the most important wallrock alterations associated with uranium mineralization [51]. It is generally considered that chloritization at the premetallogenic stage mainly distributes in the periphery of the ore body in a planar form, such as biotite-altered chlorites, which are mainly formed by alteration of ferromagnesian silicate minerals (biotite and amphibole). In this process, the Fe- and Mg-components mainly come from the wallrock itself, with little Fe- and Mg-components brought in. With the changes of environment, the temperature of the hydrothermal fluid decreases gradually, the fluid evolves to low oxygen fugacity and high sulfur fugacity, and the composition of fluid changes accordingly. The Fe- and Mg-components extracted from the wallrock enter the fluid and fill in the fissures of minerals under appropriate conditions to form vein/veinlet chlorite. Meanwhile, the hydrothermal fluid contains a certain amount of uranium, which is enriched with the precipitation of chlorite. To sum up, the relationship between chloritization and uranium mineralization in Huangsha uranium mining area is mainly related to the following four aspects:

(1) Change in the physicochemical properties of rocks.

In the process of hydrothermal alteration, such as chloritization, dolomitization, and alkali metasomatism, the interaction between hydrothermal fluids and wallrocks changes the physicochemical properties of uranium-bearing granite from hard rocks to loose and fragile rocks, and significantly increases the porosity and permeability of the rocks. This not only contributes to the reaction of hydrothermal fluids with wallrocks during the metallogenic stage, but also provides a favorable deposition environment for uranium mineralization due to the loose and fragile wallrock conditions.

(2) Indicate uranium metallogenic environment.

Various types of chlorite in Huangsha uranium mining area are iron-rich chlorites and the formation temperature ranges from 195.7 °C to 283.0 °C, with an average value of 233.2 °C, oxygen fugacity ranges from −48.0 to −41.7, with an average value of −44.2, sulfur fugacity ranges from −7.9 to −0.1, with an average value of −3.42, creating a medium-low temperature, relatively low

pH, low oxygen fugacity, and relatively high sulfur fugacity environment. The physicochemical formation conditions of various types of chlorite in this area are similar, indicating that the metallogenic environment of Huangsha uranium mining area belongs to a medium-low temperature and relatively acidic reductive environment.

(3) Change in the occurrence state of uranium in rocks.

Cheng et al (2000) [68] used a fission track method to study the Xiazhuang uranium deposit in North Guangdong Province. The results show that chlorite formed by alteration of biotite not only causes uranium to be released from uranium-bearing accessory minerals (such as monazite, xenotime, etc.) distributed in biotite, but also superimposes some uranium release in the process of biotite chloritization by adsorption. Thus, in the process of chloritization, the occurrence state of uranium in the original rock is changed. Uranium is released from uranium-bearing accessory minerals and immobile uranium (U^{4+}) is transformed into mobile uranium [U^{6+}, e.g., UO_2F_2, $(UO_2F_3)^-$, $UO_2F_4^{2-}$, $UO_2(CO_3)_4^{2-}$]. Chlorites and other clay minerals pre-enrich the released uranium, creating favorable conditions for uranium mineralization.

(4) Promotion of uranium deposition.

As mentioned above, the uranium metallogenesis in Huangsha uranium mining area was formed in a medium-low temperature and relatively acidic reduction environment. When this relatively acidic reduction environment breaks the original physicochemical equilibrium of uranium-rich fluids, uranyl and complex anions [e.g., UO_2F_2, $(UO_2F_3)^-$, $UO_2F_4^{2-}$, $UO_2(CO_3)_4^{2-}$] would be separated and further reduced and precipitated, forming uranium minerals which are dominated by tetravalent uranium (U^{4+}) [51]. In this process, the equilibrium of the uranium carrier is disrupted, resulting in uranium deposition in the uranium-rich fluids, thus forming uranium mineralization.

8. Conclusions

(1) There are five types of chlorite in Huangsha uranium mining area, including chlorite formed by the alteration of biotite, chlorite formed by the metasomatism of feldspar with Fe–Mg hydrothermal fluids, chlorite vein/veinlet filling in fissures, chlorite closely associated with uranium minerals, and chlorite transformed from clay minerals by adsorbing Mg- and Fe-components.

(2) The chlorite in Huangsha uranium mining area belongs to iron-rich chlorite and is mainly composed of chamosite, partly clinochlore, which are the products of multiple stages of hydrothermal action, and their original rocks are derived from argillite.

(3) The chlorite in the area was formed in an environment of medium-low temperature, relatively low pH, low oxygen fugacity, and relatively high sulfur fugacity. The formation mechanisms were dissolution–precipitation and dissolution–migration–precipitation. The physicochemical formation conditions for various types of chlorite in the mining area are similar, indicating that the metallogenic environment of the deposit belongs to a medium-low temperature and relatively acidic reductive environment.

(4) Chloritization is closely related to uranium mineralization. It changes the physicochemical properties of rocks, the uranium metallogenic environment, and the occurrence state of uranium in rocks, thus promoting uranium deposition.

References

1. Deer, W.A.; Howie, R.A.; Zussman, J. *Rock-Forming Minerals: Sheet Silicates*; Longman: London, UK, 1962; p. 270.
2. Caritat, P.; Hutcheon, I.; Walshe, J.L. Chlorite geothermometry: A review. *Clays Clay Miner.* **1993**, *41*, 219–239. [CrossRef]
3. Tetiker, S.; Yalcin, H.; Bozkaya, O. Approaches to the low grade metamorphic history of the Karakaya complex by chlorite mineralogy and geochemistry. *Minerals* **2015**, *5*, 221–246. [CrossRef]
4. Absar, N. Chloritization and its bearing on uranium mineralization in Madyalabodu area, Cuddapah district, Andhra Pradesh. *J. Geol. Soc. India* **2014**, *84*, 616–617. [CrossRef]
5. Zhang, Z.S.; Hua, R.M.; Ji, J.F.; Zhang, Y.C.; Guo, G.L.; Yin, Z.P. Characteristics and formation conditions of chlorite in No. 201 and No. 361 uranium deposits. *Acta Mineral. Sin.* **2007**, *27*, 161–172. (In Chinese with English Abstract).
6. Xia, F.; Meng, H.; Nie, F.J.; Yan, Z.B.; Zhang, C.Y.; Li, M.G. Characteristics of chlorite from the Nalinggou uranium deposit in the Ordos basin and its geological significance. *Acta Geol. Sin.* **2016**, *90*, 3473–3482. (In Chinese with English Abstract).
7. Cathelineau, M.; Nieva, D.A. Chlorite solid solution geothermometer the Los Azufres (Mexico) geothermal system. *Contrib. Mineral. Petrol.* **1985**, *91*, 235–244. [CrossRef]
8. Cathelineau, M. Cation site occupancy in chlorites and illites as a function of temperature. *Clay Miner.* **1988**, *23*, 471–485. [CrossRef]
9. Bryndzia, L.T.; Scott, S.D. The composition of chlorite as a function of sulfur and oxygen fugacity: An experimental study. *Am. J. Sci.* **1987**, *287*, 50–76. [CrossRef]
10. Bevins, R.E.; Robinson, D.; Rowbotham, G. Compositional variations in mafic phyllosilicates from regional low-grade metabasites and application of the chlorite geothermometer. *J. Metamorph. Geol.* **1991**, *9*, 711–721. [CrossRef]
11. Battaglia, S. Applying x-ray geothermometer diffraction to a chlorite. *Clays Clay Miner.* **1999**, *47*, 54–63. [CrossRef]
12. Grigsby, J.D. Origin and growth mechanism of authigenic chlorite in sandstones of the lower Vicksburg formation, South Texas. *J. Sediment. Res.* **2001**, *71*, 27–36. [CrossRef]
13. Gould, K.; Pe-Piper, G.; Piper, D.J.W. Relationship of diagenetic chlorite rims to depositional facies in Lower Cretaceous reservoir sandstones of the Scotian Basin. *Sedimentology* **2010**, *57*, 587–610. [CrossRef]
14. Tóth, T.; Horváth, D.; Tóth, A. Thermal effects in the density fingering of the chlorite-tetrathionate reaction. *Chem. Phys. Lett.* **2007**, *442*, 289–292. [CrossRef]
15. Mcdowell, S.D.; Elders, W.A. Authigenic layer silicate minerals in borehole Elmore 1, Salton Sea Geothermal Field, California, USA. *Contrib. Mineral. Petrol.* **1980**, *74*, 293–310. [CrossRef]
16. Hayes, J.B. Polytypism of chlorite in sedimentary rocks. *Clays Clay Miner.* **1970**, *18*, 285–306. [CrossRef]
17. Walshe, J.L. A six-component chlorite solid solution model and the conditions of chlorite formation in hydrothermal and geothermal systems. *Econ. Geol.* **1986**, *81*, 681–703. [CrossRef]
18. Hutcheon, I. Clay-carbonate reactions in the Venture area, Scotian Shelf, Nova Scotia, Canada. In *Fluid-Mineral Interactions: A Tribute to H. P. Eugster*; Spencer, R.J., Chou, I.M., Eds.; The Geochemical Society: San Antonio, TX, USA, 1990; Volume 2, pp. 199–212.
19. Rausell-Colom, J.A.; Wiewiora, A.; Matesanz, E. Relation between composition and d001 for chlorite. *Am. Mineral.* **1991**, *76*, 1373–1379.
20. Nieto, F. Chemical composition of metapelitic chlorites: X-ray diffraction and optical property approach. *Eur. J. Mineral.* **1997**, *9*, 829–842. [CrossRef]
21. Chen, Z.Y.; Huang, G.L.; Zhu, B.; Chen, Z.H.; Huang, F.; Zhao, Z.; Tian, Z.J. The characteristics and metallogenic specialization of granite-hosted uranium deposits in the Nanling region. *Geotecton. Et Metallog.* **2014**, *38*, 264–275. (In Chinese with English Abstract).
22. Shu, L.S.; Zhou, X.M.; Deng, P.; Yu, X.Q. Principal geological features of Nanling tectonic belt, South China. *Geol. Rev.* **2006**, *52*, 251–265. (In Chinese with English Abstract).
23. Mao, J.W.; Cheng, Y.B.; Chen, M.H.; Pirajno, F. Major types and time–space distribution of mesozoic ore deposits in South China and their geodynamic settings. *Miner. Depos.* **2013**, *48*, 267–294.

24. Mao, J.R.; Ye, H.M.; Liu, K.; Li, Z.L.; Takahashi, Y.; Zhao, X.L.; Kee, W.S. The Indosinian collision–extension event between the South China block and the palaeo-pacific plate: Evidence from Indosinian alkaline granitic rocks in Dashuang, Eastern Zhejiang, South China. *Lithos* **2013**, *172*, 81–97. [CrossRef]

25. Pirajno, F. *The Geology and Tectonic Settings of China's Mineral Deposits*; Springer: Berlin, Germany, 2013; pp. 127–247.

26. Shu, T.T.; Zhong, F.J.; Qi, J.M.; Wu, D.H.; Mou, P. Geological characteristics of mineralization of Huangsha uranium deposit of "intersection" type in Qingzhangshan pluton. *Miner. Resour. Geol.* **2017**, *31*, 306–311. (In Chinese with English Abstract).

27. Zhang, W.L.; Chen, L.M.; Dang, F.P.; Fan, Z.Q.; Gao, M.Q. A study of ore-controlling mechanism of fault depression belt: A case study on Huangsha uranium mining area in South Jiangxi. *Miner. Resour. Geol.* **2016**, *30*, 746–751. (In Chinese with English Abstract).

28. Dang, F.P.; Chen, L.M.; Li, Z.P.; Xu, P.L.; Cai, C.H.; Fan, Z.Q. Structural characteristics of Shangjiao section and direction of deep prospecting in the Huangsha uranium mining area, Southern Jiangxi province. *Geol. Explor.* **2017**, *53*, 624–631. (In Chinese with English Abstract).

29. Mou, P.; Pan, J.Y.; Huang, G.W.; Zhong, F.J.; Liu, T.T.; Meng, H. Geochemical characteristics of trace elements and its significance in uranium deposit 221, Huangsha uranium ore district. *Sci. Technol. Eng.* **2016**, *16*, 27–33. (In Chinese with English Abstract).

30. Wu, D.H.; Pan, J.Y.; Xia, F.; Zhong, F.J.; Guang, W.H.; Qi, J.M.; Hong, B.Y. Trace elements geochemical characteristics and metallogenic model of the Shangjiao uranium deposit in Southern Jiangxi. *Acta Petrol. Et Mineral.* **2018**, *37*, 590–604. (In Chinese with English Abstract).

31. Yan, D.P.; Zhou, M.F.; Song, H.L.; Wang, X.W.; Malpas, J. Originand tectonic significance of a Mesozoic multi-layer over-thrust within the Yangtze block (South China). *Tectonophysics* **2003**, *3*, 239–254. [CrossRef]

32. Zhang, Z.H.; Zhang, B.T. *Research of Uranium-Bearing Granites and Their Related Uranium Deposits in South China*; Atomic Energy Press: Beijing, China, 1991; pp. 13–15. (In Chinese)

33. Tao, J.H.; Li, W.X.; Li, X.H.; Cen, T. Petrogenesis of early Yanshanian highly evolved granites in the Longyuanba area, Southern Jiangxi province:evidence from zircon U-Pb dating, Hf-O isotope and whole-rock geochemistry. *Sci. China* **2013**, *56*, 922–939. [CrossRef]

34. Zhang, M.; Chen, P.R.; Huang, G.L.; Ling, H.F. The research on the geochemical characteristics of Longyuanba composite pluton in Nanling region. *Uranium Geol.* **2006**, *22*, 336–344. (In Chinese with English Abstract).

35. Zhang, M.; Chen, P.R.; Huang, G.L.; Tan, Z.Z.; Ling, H.F.; Chen, W.F. Single-zircon La-ICP-MS ages of the Longyuanba pluton in the Eastern Nanling region and geological implication. *Acta Geol. Sin.* **2006**, *80*, 984–994. (In Chinese with English Abstract).

36. He, Z.Y.; Xu, X.S.; Niu, Y. Petrogenesis and tectonic significance of a Mesozoic granite–syenite–gabbro association from inland South China. *Lithos* **2010**, *119*, 621–641. [CrossRef]

37. Gao, P.; Zhao, Z.F.; Zheng, Y.F. Magma mixing in granite petrogenesis: Insights from biotite inclusions in quartz and feldspar of Mesozoic granites from South China. *J. Asian Earth Sci.* **2016**, *123*, 142–161. [CrossRef]

38. Wang, L.X.; Ma, C.Q.; Lai, Z.X.; Marks, M.A.W.; Zhang, C.; Zhong, Y.F. Early Jurassic mafic dykes from the Xiazhuang ore district (South China): Implications for tectonic evolution and uranium metallogenesis. *Lithos* **2015**, *239*, 71–85. [CrossRef]

39. Bonnetti, C.; Liu, X.; Mercadier, J.; Cuney, M.; Deloule, E.; Villeneuve, J.; Liu, W.Q. The genesis of granite-related hydrothermal uranium deposits in the Xiazhuang and Zhuguang ore fields, North Guangdong province, SE China: Insights from mineralogical, trace elements and U-Pb isotopes signatures of the U mineralisation. *Ore Geol. Rev.* **2018**, *92*, 588–612. [CrossRef]

40. Liu, G.Q.; Zhao, K.D.; Jiang, S.Y.; Chen, W. In-situ sulfur isotope and trace element analysis of pyrite from the Xiwang uranium ore deposit in South China: Implication for ore genesis. *J. Geochem. Explor.* **2018**, *195*, 49–65. [CrossRef]

41. Zhou, J.X. *Quantitative Analysis of Silicate Minerals by Electron Probe Method*; Standards Press of China: Beijing, China, 2002; pp. 1–8. (In Chinese)

42. Zheng, Q.L. Calculation of the Fe^{3+} and Fe^{2+} contents in silicate and Ti-Fe oxide minerals from EPMA date. *Acta Mineral. Sin.* **1983**, *1*, 55–62. (In Chinese with English Abstract).

43. Foster, M.D. *Interpretation of the Composition and a Classification of the Chlorites*; US Geology Survey Professional Paper, 414A; US Government Printing Office: Washington, DC, USA, 1962; pp. 1–30.

44. Hillier, S.; Velde, B. Octahedral occupancy and the chemical composition of diagenetic (low-temperature) chlorites. *Clay Miner.* **1991**, *26*, 149–168. [CrossRef]

45. Zang, W.; Fyfe, W.S. Chloritization of the hydrothermally altered bedrock at the Igarapé Bahia gold deposit, Carajás, Brazil. *Miner. Depos.* **1995**, *30*, 30–38. [CrossRef]

46. Li, R.Z.; Liu, C.D.; Liang, L.; Kong, M.; Wang, B.; Wan, J.J. Characteristics and geological significance of chlorite from the Dafushang uranium deposit in Taoshan area, Jiangxi Province. *Acta Petrol. Et Mineral.* **2016**, *35*, 297–305. (In Chinese with English Abstract).

47. Li, H.D.; Pan, J.Y.; Liu, W.Q.; Jiang, W.B.; Li, J.; Liang, Y.Y.; Xie, Q.; Lu, Y. Mineral characteristics and geological significance of chlorite from the Julong'an uranium deposit in Le'an, Jiangxi Province. *Acta Petrol. Et Mineral.* **2017**, *36*, 535–548. (In Chinese with English Abstract).

48. Hey, M.H. A New Review of the Chlorites. *Mineral. Mag.* **1954**, *30*, 278–292. [CrossRef]

49. Zane, A.; Weiss, Z. A procedure for classifying rock-forming chlorites based on microprobe data. *Rend. Lincei* **1998**, *9*, 51–56. [CrossRef]

50. Inoue, A. Formation of clay minerals in hydrothermal environments. In *Origin and Mineralogy of Clays*; Velde, B., Ed.; Springer: Berlin, Germany, 1995; pp. 268–301.

51. Guo, G.L.; Liu, X.D.; Pan, J.Y.; Zhang, Z.S.; Li, X.B. Character of chlorite and its relationship to uranium mineralization in uranium deposit No.302. *Uranium Geol.* **2012**, *28*, 35–41. (In Chinese with English Abstract).

52. Zhang, L.; Chen, Z.Y.; Tian, Z.J.; Huang, G.L.; Tian, X.L. Chemical composition of biotite and chlorite in the uranium-bearing and barren granites, Northern Guangdong Province, South China: Implications for uranium mineralization. *Earth Sci. Front.* **2017**, *24*, 62–75. (In Chinese with English Abstract).

53. Nutt, C.J. Chloritization and associated alteration at the Jabiluka unconformity-type uranium deposit, Northern Territory, Australia. *Can. Mineral.* **1989**, *27*, 41–58.

54. Alexandre, P.; Kyser, K.; Polito, P. Alteration Mineralogy and Stable Isotope Geochemistry of Paleoproterozoic BasementHosted Unconformity-Type Uranium Deposits in the Athabasca Basin, Canada. *Econ. Geol.* **2005**, *100*, 1547–1563. [CrossRef]

55. Alexandre, P.; Kyser, K.; Jiricka, D.; Witt, G. Formation & Evolution of the Centennial Unconformity-Related Uranium Deposit in the South-Central Athabasca Basin, Canada. *Econ. Geol.* **2012**, *107*, 385–400.

56. Wiewióra, A. Crystallochemical classifications of phyllosilicates based on the unified system of projection of chemical composition: I. the mica group. *Clay Miner.* **1990**, *25*, 73–81. [CrossRef]

57. Laird, J. Chlorites; metamorphic petrology. *Rev. Mineral. Geochem.* **1988**, *19*, 405–453.

58. Sun, T.; Zhou, X.M.; Chen, P.L.; Li, H.M.; Zhou, H.Y.; Wang, Z.C.; Shen, W.Z. Strongly peraluminous granites of Mesozoic in Eastern Nanling Range, Southern China: Petrogenesis and implications for tectonics. *Sci. China* **2005**, *48*, 23–32. [CrossRef]

59. Xie, X.G.; Byerly, G.R.; Ferrell, J.R.E. IIb trioctahedral chlorite from the Barberton greenstone belt: Crystal structure and rock composition constraints with implications to geothermometry. *Contrib. Mineral. Petrol.* **1997**, *126*, 275–291. [CrossRef]

60. Hua, R.M.; Li, X.F.; Zhang, K.P.; Ji, J.F.; Zhang, W.L. Characteristics of clay minerals derived from hydrothermal alteration in Jinshan gold deposit: Implication for the environment of water-rock interaction. *Acta Mineral. Sin.* **2003**, *23*, 23–30. (In Chinese with English Abstract).

61. Guo, G.L.; Liu, X.D.; Pan, J.Y.; Liu, C.D.; Yan, Z.B.; Chen, Y.P. Study of fluid inclusion from uranium deposit No.302 in north Guangdong. *Uranium Geol.* **2010**, *26*, 350–354. (In Chinese with English Abstract).

62. Zhang, W.; Zhang, S.T.; Cao, H.W.; Wu, J.D.; Xiao, C.X.; Chen, H.J.; Tang, L. Characteristics of chlorite minerals from Xiaolonghe tin deposit in West Yunan, China and their geological omplication. *J. Chengdu Univ. Technol.* **2014**, *41*, 318–328. (In Chinese with English Abstract).

63. Ling, H.F. Origin of hydrothermal fluids of granite-type uranium deposits: Constraints from redox conditions. *Geol. Rev.* **2011**, *2*, 193–206. (In Chinese with English Abstract).

64. Zhang, G.; Wasyliuk, K.; Pan, Y. The characterization and quantitative analysis of clay minerals in the Athabasca Basin, Saskatchewan: Application of short-wave infrared reflectance spectroscopy. *Can. Mineral.* **2001**, *39*, 1347–1363. [CrossRef]

65. Eugster, H.P.; Wones, D.R. Stability relations of the ferruginous biotite, annite. *J. Petrol.* **1962**, *1*, 82–125. [CrossRef]

66. Liu, Y.P.; Zhang, S.Y.; Zhang, H.F. Advances on Mineral Genesis of Chlorite: A Review. *Adv. Geosci.* **2016**, *3*, 264–282. (In Chinese with English Abstract). [CrossRef]

67. Liu, Y.J.; Cao, L.M. *Element Geochemistry Principle*; Geological Publishing House: Beijing, China, 1987; pp. 124–128. (In Chinese)

68. Cheng, H.H.; Ma, H.F.; Xiang, W.D. Study on changes of existing state of uranium during alkalic metasomatism using fission-track method. *Uranium Geol.* **2000**, *16*, 291–296. (In Chinese with English Abstract).